Deformation Mechanisms and Strain Storage During Forging of Powder-Metallurgy Nickel-base Turbine Disk Alloy

By

Wen J. Tu

A dissertation submitted in partial fulfillment
of the requirements for the degree of
Doctor of Philosophy
(Materials Science and Engineering)
in The University of Michigan
2010

Doctoral Committee:

Professor Tresa M. Pollock, Co-Chair
Professor J. Wayne Jones, Co-Chair
Professor Gary S. Was
Assistant Professor Samantha H. Daly

To my parents

and

To God

Acknowledgements

There are a large number of individuals who have made it possible for me to complete the work for this thesis. I would like to acknowledge the following people for their assistance and support.

First, I would like to thank my adviser, Professor Tresa M. Pollock, for her guidance, assistance, motivation, and belief in me. Her guidance was absolutely vital for my development as a scientist and engineer for my career at the University of Michigan. I am honored and consider myself very fortunate to have been a part of her research group, which is composed of the brightest of individuals. Her love and knowledge of engineering will be inspiring for the rest of my career.

I would also like to acknowledge past and present members of the Pollock and Jones group who have enriched my daily time in the lab. Special thanks go to Chris Torbet who has always been an insightful, knowledgeable, innovative, and willing guide for everything lab-related. Special thanks also go to my lab-mates Sara Perez-Bergquist, and Mclean Echlin, whose friendships and daily conversations made my time in the lab insightful and enjoyable. And to the rest of the Pollock and Jones group, who were always willing to share knowledge and experiences, thank you.

I would also like to thank Eric Payton, Professor Michael J. Mills, and Professor Yunzhi Wang for their collaborations in this work.

Also, the support for this work provided by GE Aviation, through the USA program is gratefully acknowledged.

Table of Contents

Dedication....ii
Acknowledgements....iii
List of Figures....vii

Chapter 1. Introduction....1

Chapter 2. Background....4
2.1. Cast and Wrought Billet Processing....5
2.2. Powder Metallurgy Processing....5
2.3. Isothermal Forging....7
2.3.1. Superplasticity....8
2.3.2. Grain Growth....12
2.3.2.1. Normal Grain Growth....13
2.3.2.2. Grain Growth Inhibition....16
2.3.2.3. Superplasticity Enhanced Grain Growth....17
2.3.2.4. Abnormal Grain Growth....19
2.3.3. Static Recrystallization....21
2.3.4. Dynamic Recrystallization....24
2.4. Heat Treatments....26
2.5. René 88DT Microstructure....27
2.6. Chapter Summary....29

Chapter 3. Local Strain Distribution on the Super-granular Scale....30
3.1. Strain Mapping Experimental Procedure....31
3.1.1. Sample Frabrication....31
3.1.2. Grid Deoposition and Marker Identification....31
3.1.3. Compression Testing for Strain Mapping....32
3.2. Experimental Results....34
3.3. Discussion and Summary....37

Chapter 4. Flow Stress Evolution During High Temperature Compression....39
4.1. Experimental Procedures....39
4.2. Experimental Results....40
4.3. Discussion....45
4.4. Chapter Summary....48

Chapter 5. Microstructural Evolution During High Temperature Compression....49

5.1. Experimental Procedures....49
5.1.1. EBSD Sample Preparation....51
5.1.2. EBSD Grain Size Measurement....52
5.2. Microstructural Evolution During Thermal Transients....53
5.2.1. Experimental Results....53
5.2.2. Discussion....56
5.2.2.1. Equilibrium γ' Volume Fraction....57
5.2.2.2. γ' Dissolution Rate....58
5.3. Temperature and Strain Rate Dependent Microstructural Evolution....58
5.3.1. Experimental Results....59
5.3.2. Discussion....65
5.3.2.1. Slow Strain Rate Grain Size Distribution....66
5.3.2.2. γ' Coarsening Rate....66
5.3.2.3. The γ Grain Size: the Zener Limit....67
5.3.2.4. Evolution of Grain Twinning....68
5.3.2.5. Dynamic Recrystallization During High Strain Rates....70
5.4. Strain Dependent Microstructural Evolution....71
5.4.1. Experimental Results....72
5.4.2. Discussion....76
5.5. Superplasticity Enhanced Grain Growth....77
5.5.1. Experimental Results....77
5.5.2. Discussion....78
5.6. Chapter Summary....78

Chapter 6. Sub-granular Scale Misorientation and Strain Accommodation....81
6.1. Experimental Procedure....82
6.2. Temperature and Strain Rate Varying Misorientation Evolution....83
6.2.1. Experimental Results....83
6.2.1.1. Measured Misorientation....83
6.2.1.2. GAM Distributions....87
6.2.1.3. Grain Size Dependence of Average Misorientation....91
6.2.1.4. Taylor Factor....95
6.2.2. Discussion....95
6.3. Strain Rate Dependence of Misorientation Accumulation....98
6.3.1. Experimental Results....98
6.3.1.1. Average Misorientation Accumulation....98
6.3.1.2. GAM Distribution Analysis....99
6.3.2. Discussion....101
6.4. Strain Varying Misorientation Evolution....102
6.4.1. Experimental Results....102
6.4.2. Discussion....107
6.5. Chapter Summary....110

Chapter 7. Deformation Mechanism Models....113
7.1. Superplasticity Enhanced Grain Growth....113
7.1.1. Grain Growth with Zener Drag....113

7.1.2. Atomic Diffusivity....115
7.1.3. Model Grain Growth Predictions....118
7.1.4. Discussion....120
7.2. Boundaries of Superplasticity....121
7.2.1. Grain Boundary Diffusion Coefficient....121
7.2.2. Analysis of Experimental Data....122
7.2.3. Discussion....124
7.3. Deformation Mechanisms by Grain Fraction....125
7.3.1. Discussion....127
7.4. Average Grain Size by Deformation Mechanism....128
7.5. Chapter Summary....130

Chapter 8. EBSD Misorientation and Dislocation Density....132
8.1. Relationship Between KAM and Dislocation Density....133
8.2. KAM Dislocation Density Calculations....135
8.3. Flow Stress Correlation Dislocation Density....137
8.3.1. Plasticity and Dislocation Density....138
8.3.2. Strengthening Contributions of René 88DT....139
8.3.3. Dislocation Density Comparisons....139
8.4. Discussion....141
8.4.1. Factors Affecting Dislocation Density Estimation....142

Chapter 9. Summary and Future Work....143
9.1. Future Work....146

References....150

List of Figures

Figure 2.1: Illustration of grain switching event during superplastic deformation.....9

Figure 2.2: Theoretical region of abnormal grain growth with mean misorientation angle of 5 degrees.....20

Figure 2.3: Theoretical regions of abnormal grain growth with variations in Z and mean misorientation angle.....21

Figure 2.4: Isothermal recrystallization kinetics showing fraction recrystallized as a function of time.....23

Figure 2.5: as-extruded René 88DT microstructure with preferential etching of γ'...28

Figure 2.6: microstructure of René 88DT (a) as-extruded (b) as-forged (c) as heat treated and aged.....28

Figure 3.1: Sample surface Pt grid markers before compression.....32

Figure 3.2: Induction heating profile sample for compression tests with 4mm diameter 7mm height sample.....33

Figure 3.3: Compression Set-up.....33

Figure 3.4: Von Mises strain map for sample compressed at 0.00032/s to 14.5% strain. Scale bar in percent Von Mises strain.....34

Figure 3.5: BSE SEM image of large grain with low strain surrounded by highly deformed grains after compression on right compared to representative strain map of area around a similar large grain. Compression at 0.001/s strain rate to 0.228 engineering strain.....35

Figure 3.6: Microstructure of strained René88DT shows grain boundary offsets for superplastic deformation. (a) 0.05 strain, 0.032/s. (b) 0.05 strain, 0.0032/s.....36

Figure 3.7: Von Mises strain distribution for 0.1 strain at 0.00032/s strain rate. Different colors indicate different samples. Black line with areos indicates where FWHM is measured.....37

Figure 3.8: Full-width half-max of strain distributions for all René88DT strain maps. Y-axis is width of normalized strain distribution, such as shown in Figure 3.7.....37

Figure 4.1: True stress strain curves for René 88DT compressed at 4 different strain rates, all at 1241K (968˚C).....41

Figure 4.2: True stress strain curves for René 88DT compressed at 4 different strain rates, all at 1269K (996˚C).....41

Figure 4.3: True stress strain curves for René 88DT compressed at 4 different strain rates, all at 1298K (1025˚C).....42

Figure 4.4: True stress strain curves for René 88DT compressed at 4 different strain rates, all at 1323K (1050˚C).....42

Figure 4.5: True Stress-strain curves for René 88DT compressed at different strain rates all at a temperature of 1298K (1025˚C).....44

Figure 4.6: Ratio of flow stress at 110% true train to yield stress for René 88DT compressed at different strain rates all at 1269K (996˚C).....44

Figure 4.7: Adiabatic flow stress at 70% true strain for René 88DT compressed at different strain rate and temperatures.....45

Figure 5.1: Schematic of EBSD system.....50

Figure 5.2: Inverse pole figure (IPF) plot of as-extruded René 88DT.....54

Figure 5.3: IPF maps showing René 88DT microstructure after ramp-up to target temperature before deformation.....54

Figure 5.4: Average grain diameter of pre-deformation samples. As-extruded grain size is indicated by red line.....55

Figure 5.5: Grain diameter distribution of as-extruded René 88DT compared to pre-deformation samples of different temperatures.....55

Figure 5.6: Fraction of grains twinned as a function of pre-deformation temperature. As-extruded level shown by red line.....56

Figure 5.7: Area fraction of grains untwinned as a function of pre-deformation temperature. As-extruded level shown by red line.....56

Figure 5.8: René 88DT equilibrium γ’ volume fraction as a function of temperature. Red box outlines testing temperatures.....57

Figure 5.9: IPF plot of René 88DT compressed at 4 different temperatures with 4 different strain rates, as labeled by the vertical and horizontal axis respectively. The as-extruded IPF plot of shown on the right side.....60

Figure 5.10: Average grain diameter of René 88DT plotted as a function of compression strain rate for varying test temperatures. As-extruded average grain diameter is indicated by dashed red line.....60

Figure 5.11: Grain diameter distribution for René 88DT compressed at 1241K (968˚C).....61

Figure 5.12: Grain diameter distribution for René 88DT compressed at 1269K (996˚C).....61

Figure 5.13: Grain diameter distribution for René 88DT compressed at 1298K (1025˚C).....62

Figure 5.14: Grain diameter distribution for René 88DT compressed at 1323K (1050˚C).....62

Figure 5.15: Fraction of grains containing twins of René 88DT after deformation at various temperatures and strain rate. Imposed strain is 110% true strain. As-extruded level is shown by red line.....63

Figure 5.16: Area fraction of René 88DT containing twins after deformation at various temperatures and strain rates. Imposed strain is 110% true strain. As-extruded level is indicated by red line.....64

Figure 5.17: Average grain diameter of twinned and untwinned grains compressed at 1241K (968˚C).....64

Figure 5.18: Average grain diameter of twinned and untwinned grains compressed at 1269K (996˚C).....64

Figure 5.19: Average grain diameter of twinned and untwinned grains compressed at 1298K (1025˚C).....65

Figure 5.20: Average grain diameter of twinned and untwinned grains compressed at 1323K (1050˚C).....65

Figure 5.21: Primary γ' coarsening rate of René 88DT according to LSW-type coarsening equation presented by E. Payton.....67

Figure 5.22: René 88DT Zener limit γ grain size as a function of temperature dependent equilibrium γ' volume fraction. Red box outlines test temperature range.68

Figure 5.23: Fraction of grains containing twins as a function of strain rate for René 88DT compressed at 1298˚K (1025˚C).....69

Figure 5.24: Zener limit of γ grain size as a function of temperature assuming that equilibrium γ' volume fraction has been reached compared to the average grain size of twinned grains after deformation at 0.00032/s strain rate at various temperatures.70

Figure 5.25: IPF plot of René 88DT compressed at different strain rates to different engineering strain. All samples test temperature is 1298K (1025˚C). The as-extruded microstructure is shown on the right.....73

Figure 5.26: Average grain diameter as a function of engineering strain for René 88DT compressed at varying strain rates at 1298K (1025˚C).....73

Figure 5.27: Fraction of grains containing twins as a function of engineering strain for René 88DT compressed at varying strain rates at 1298K (1025˚C).....74

Figure 5.28: Average grain diameter twinned and untwinned grains as a function of strain for René 88DT compressed at 0.001/s at 1298K (1025˚C).....75

Figure 5.29: Average grain diameter twinned and untwinned grains as a function of strain for René 88DT compressed at 0.0055/s at 1298K (1025˚C).....75

Figure 5.30: Average grain diameter twinned and untwinned grains as a function of strain for René 88DT compressed at 0.018/s at 1298K (1025˚C).....75

Figure 5.31: Average grain diameter twinned and untwinned grains as a function of strain for René 88DT compressed at 0.05/s at 1298K (1025˚C).....76

Figure 5.32: Time interval grain size evolution during compression at different superplastic strain rates.....77

Figure 6.1: GROD Map of René 88DT compressed at different temperature and strain rate. As-extruded GROD is shown on the right along with GROD scale.....85

Figure 6.2: Average grain orientation spread as a function of strain rate for René 88DT compressed at different temperatures. Red line shows average pre-deformation GOS.....85

Figure 6.3: KAM Map of René 88DT compressed at different temperature and strain rate. As-extruded KAM is shown on the right along with scale.....86

Figure 6.4: Local KAM region showing misorientation substructure within grains as indicated by bands of high KAM in green and red.....86

Figure 6.5: Average KAM as a function of strain rate for René 88DT compressed at different temperatures.....87

Figure 6.6: GAM as a function of strain rate for René 88DT compressed at different temperatures.....87

Figure 6.7: GAM distribution for René 88DT compressed at 1241˚K (968˚C).....88

Figure 6.8: GAM distribution for René 88DT compressed at 1269˚K (996˚C).....88

Figure 6.9: GAM distribution for René 88DT compressed at 1298˚K (1025˚C).....89

Figure 6.10: GAM distribution for René 88DT compressed at 1323˚K (1050˚C).....89

Figure 6.11: Experimental GAM distribution of René 88DT compressed at 1241K (968˚C) using 0.032/s strain rate compared to the Log-Lorentzian distribution fit....89

Figure 6.12: Log-Lorentzian distribution standard deviation for GAM distribution fits as a function of strain rate for various temperatures.....90

Figure 6.13: Log-Lorentzian distribution amplitude (A) for GAM distribution fits as a function of strain rate for various temperatures.....90

Figure 6.14: Log-Lorentzian distribution peak position (x_0) for GAM distribution fits as a function of strain rate for various temperatures.....91

Figure 6.15: Average GAM as a function of grain size for the as-extruded René 88DT material.....92

Figure 6.16: Plots of GAM as a function of grain size for René 88DT samples compressed at 4 different strain rates, all at 1241K (968˚C).....93

Figure 6.17: Plots of GAM as a function of grain size for René 88DT samples compressed at 4 different strain rates, all at 1269K (996˚C).....93

Figure 6.18: Plots of GAM as a function of grain size for René 88DT samples compressed at 4 different strain rates, all at 1298K (1025˚C).....94

Figure 6.19: Plots of GAM as a function of grain size for René 88DT samples compressed at 4 different strain rates, all at 1323K (1050˚C).....94

Figure 6.20: GROD and Taylor factor maps for samples compressed at 2 different strain rates and temperatures as labeled on top of each map.....95

Figure 6.21: Grain orientation spread (GOS) of René 88DT samples compressed at various strain rates at 1298K (1025˚C). Red line indicates the pre-deformation level.....98

Figure 6.22: Average KAM for René 88DT compressed at various strain rates at 1298K (1025˚C). Red line indicates the pre-deformation level.....99

Figure 6.23: Average GAM for René 88DT compressed at various strain rates at 1298K (1025˚C). Red line indicates the pre-deformation level.....99

Figure 6.24: Standard deviation (S) of Log-Lorentzian fit of GAM distribution for samples compressed at 1298K (1025˚C). Red line indicates the pre-deformation level.....100

Figure 6.25: Amplitude (A) of Log-Lorentzian fit of GAM distribution for samples compressed at 1298K (1025˚C). Red line indicates the pre-deformation level.....100

Figure 6.26: Position parameter (x_0) of Log-Lorentzian fit of GAM distribution for samples compressed at 1298K (1025˚C). Red line indicates the pre-deformation level.....100

Figure 6.27: Average GOS of René 88DT samples compressed at different strain rates in 0.1 strain increments.....103

Figure 6.28: Average KAM of René 88DT samples compressed at different strain rates in 0.1 strain increments.....103

Figure 6.29: Average KAM of René 88DT samples compressed at different strain rates in 0.1 strain increments.....104

Figure 6.30: GAM as a function of grain size for René 88DT samples compressed at 0.001/s to e = 0.1 increments at 1298K (1025˚C).....105

Figure 6.31: GAM as a function of grain size for René 88DT samples compressed at 0.0055/s to e = 0.1 increments at 1298K (1025˚C).....106

Figure 6.32: GAM as a function of grain size for René 88DT samples compressed at 0.018/s to e = 0.1 increments at 1298K (1025˚C).....107

Figure 6.33: GAM as a function of grain size for René 88DT samples compressed at 0.05/s to e = 0.1 increments at 1298K (1025˚C).....107

Figure 7.1: Excess vacancy concentration created near the grain boundaries during grain boundary sliding as a function of strain for various strain rates.....117

Figure 7.2: Atomic diffusivity as a function of strain for various superplastic strain rates at 1298K (1025˚C).....117

Figure 7.3: Atomic Diffusivity of René 88DT during deformation at 0.001/s at various temperatures as a function of true strain.....118

Figure 7.4: Grain diameter ratio of initial to current as a function of time for René 88DT deformed at various superplastic strain rates at 1298K (1025˚C).....119

Figure 7.5: Grain diameter ratio of initial to time dependent grain size as a function of time for René 88DT deformed at 0.001/s at 1298K (1025˚C).....119

Figure 7.6: Grain diameter ratio of initial to time dependent grain size as a function of time for René 88DT deformed at 0.002/s at 1298K (1025˚C).....120

Figure 7.7: Plot of normalized flow stress vs. normalized grain size, temperature, and strain rate showing deviation of experimental data from solution, which satisfies superplastic deformation.....123

Figure 7.8: Boundaries of superplasticity as a function of grain size, strain rate, and temperature. The area below the 3D surface is where superplasticity dominates.....124

Figure 7.9: Maximum superplastic grain size as a function of strain rate for René 88DT deformed at René 88DT.....125

Figure 7.10: Fraction of grains above maximum superplastic grain size for samples deformed at various strain rates at various temperatures.....126

Figure 7.11: Fraction of grains above d_{max} as a function of strain for 4 different strain rates at 1298K (1025˚C).....126

Figure 7.12: Average GAM of power-law creep grains and superplastic grains as a function of strain rate for René 88DT deformed to 110% true strain at 1298K (1025˚C).....127

Figure 7.13: Average grain size of superplastic grains for René 88DT deformed at various strain rate at various temperatures.....129

Figure 7.14: Average grain size of power-law creep grains for René 88DT deformed at various strain rate at various temperatures.....129

Figure 7.15: Average grain size of power-law creep grains for René 88DT deformed at various strain rate at 1298K (1025˚C) with saturation grain size solution fit.....130

Figure 8.1: Regular pattern of EBSD scan points over representative microstructure. KAM of the red scan point is the average misorientation from its neighboring points.....133

Figure 8.2: Schematic of relationship between an array of edge dislocations and lattice strain in degrees.....134

Figure 8.3: EBSD calculated dislocation density as a function of strain rate for René 88DT compressed to 1.1 true strain at 1298K (1025°C). As-extruded dislocation density is indicated by red line.....136

Figure 8.4: KAM calculated dislocation density as a function of strain rate for René 88DT compressed to 1.1 true strain at various temperatures.....137

Figure 8.5: KAM calculated dislocation density compared to flow stress correlated dislocation density as a function of strain rate for René 88DT compressed at 1298K (1025°C).....140

Figure 9.1: Flow chart describing the steps taken in the complete analysis of René 88DT microstructure evolution during high temperature compression along with the section it is described in this study. The final average grain size for each group of grains highlighted in red can be averaged to give a total average grain size for René 88DT post-deformation.....145

Chapter 1

Introduction

High temperature gas turbines generate energy by directing a combusted mixture of fuel and compressed air over turbine blades, therefore spinning the turbines. The energy extracted in the form of shaft power, compressed air, and thrust are used to power turbines for propulsion and energy generation. The turbine blades are connected to turbine disks within gas turbines. Due to the violent nature of the combustion process, turbine disks work under extreme conditions, experiencing high temperature and large stresses. Nevertheless, these components are expected not to fail over the lifetime of the engines. Furthermore, since the efficiency of the engines increase with increasing temperature, the disks are pushed to their material capability limits.

Turbine disks of current combustion turbines are generally made from nickel-base superalloys because of the need for high temperature strength along with high creep, corrosion, and fatigue resistance. Turbine engine manufacturers produce polycrystalline disk alloys with well-controlled chemistry, grain structure, and mechanical properties in order to extend operational lifetimes and increase engine efficiency. However, the complications of grain structure control and its resultant influence on design and processing of disk materials makes optimization of current

and new disk materials time consuming and expensive. To reduce qualification time for disk materials and processing, aircraft engine manufacturers need to develop accurate constitutive models with embedded information on microstructure evolution during fabrication and processing. Currently, there is a lack of understanding of the effects of thermo-mechanical processing on the microstructure of these alloys. The goal of this research is to quantify the driving forces for microstructural evolution during forging and to predict the material response to varying forging conditions. This goal can be separated into four distinct objectives to:

1. Identify straining mechanisms during compressive deformation at conditions that correspond to simulated forging.
2. Characterize the evolution of microstructure during high temperature compression.
3. Quantify grain scale strain accommodation and storage processes.
4. Model deformation mechanisms and the corresponding microstructural response.

The alloy of interest in this study is a powder metallurgy turbine disk alloy developed by GE Aviation named René 88DT [1], which has been in use in commercial jet engines for the last decade. This study was conducted in parallel with a complementary effort at the Ohio State University [2] on microstructural evolution in René 88DT during processing. The focus of this study was on the microstructural evolution during isothermal forging, while the OSU effort focused on the microstructure evolution during subsequent high temperature heat treatments of the same alloy.

Chapter 2 will highlight the thermomechanical processing of Ni-base superalloys such as René 88DT and also describe the underlying physical mechanisms that contribute to microstructural evolution during processing. In the subsequent chapters, new methods for grain structure, strain accommodation, and strain storage analysis will be presented. Detailed analysis of René 88DT using these methods will be reported and discussed. In chapters 7 and 8, new models describing deformation mechanisms and grain structure evolution will be presented and subsequently discussed.

Chapter 2

Background

Ni-based superalloys are developed to have superior performance in high stress/temperature applications. They are strengthened by γ' (Ni_3Al) precipitates and by addition of molybdenum, tungsten, cobalt, and other elements in solid solution. The ability of Ni-superalloys to withstand high temperature and stress has lead to their use in many sections of the aircraft engine, such as combustors, nozzles, turbine blades and turbine disks. Alloys used to make turbine disks have undergone the most advancement because of the extreme conditions they endure during engine operation. Further development of disk alloys without drastic increases in production costs have been slow because of the difficulties in alloying arising from increased levels of refractory additions that cause increasing micro-segregation and defects in large ingots [3]. Furthermore, increases in strength of these disk alloys are concurrent with adverse decreases in hot workability, making the alloys extremely hard and expensive to shape. The demand for improved jet engine efficiency and performance without increasing production costs has driven the development of powder metallurgy (PM) techniques for producing turbine disks of highly alloyed material of desired microstructure, properties, and cost efficiency. The next sections describe the thermo-mechanical processes that powder superalloys go through before use and the

underlying physical mechanisms that drive microstructural evolution during processing.

2.1 Cast and Wrought Billet (CW) Processing

Ingot metallurgy processing has been the traditional method for production of disk alloy materials. Working of cast ingots into refined billets has worked well for many simple nickel based superalloys. In more complex alloy systems, casting large ingots inevitably results in segregation and the formation of non-equilibrium phases, which may be detrimental to mechanical properties [3]. Chemical inhomogeneity due to segregation may also result in variations of local transformation temperatures and subsequent variations in grain sizes. Gamma-prime (γ') is the second phase used in many nickel-based superalloys to control grain size by grain boundary pinning. Variation in local γ' solvus due to chemical inhomogeneity results in local variations in γ' content. If near-solvus processing is used during forging or heat treatment operations on segregated material, local γ' solvus temperatures can be exceeded and rapid localized grain growth may occur, resulting in a mixture of grain sizes and/or bands of fine and coarse grains [3].

2.2 Powder Metallurgy (PM) Processing

Superalloy technology evolved toward powder metallurgy because higher alloy content materials were desired while processing by traditional cast and wrought routes were difficult due to segregation and workability issues. The process of PM superalloy production has evolved immensely since the onset of early experiments. Inert gas atomization, the most common method of powder production, starts with the melting of pre-alloyed cast ingot by vacuum induction heating, then uses

impingement of high velocity argon gas jets on a molten material stream to produce fine powders, which solidify during free fall in the atomization tower. The powder particle size depends on surface tension, viscosity, and density of the liquid metal, as well as the velocity of the gas stream [4]. The molten material from which the metal powder is made is much more homogenized than tradition CW ingots, therefore producing powder that is also very homogenized.

After superalloy powder is produced, it is classified by sieving through screens of exact mesh sizes. Powder size to a large extent controls life-cycle fatigue characteristics; the powder size or mesh fraction is a key factor in inclusion content of the material and therefore controls fatigue life capability and allowable service stresses. Early PM efforts used <250μm (-60 mesh) and then <106μm (-140 mesh), and finally the mesh size evolved to <53μm (-270 mesh), which is used for the production of René 88DT [3]. After screening, the powder is vacuum loaded into a container ready for consolidation.

Superalloy powders are consolidated to full density using a combination of high temperature and high pressure by hot isostatic pressing (HIP), hot compaction, extrusion, or a combination of these processes. HIP is a process in which high-pressure gas, such as argon, is applied to the alloy powder at high temperatures to consolidate the powder. The containers that can be simple geometric shapes or complex near-net shapes. The resulting product can be a billet suitable for subsequent extrusions and/or forging. The HIP product can also be a near-net forging preform that can be used without additional hot working. The HIP processing parameters are generally between 1313 to 1523K (1040 to 1250°C) and 105 to 205 MPa (15 to 30

ksi) for 3 to 5 hours [4]. Current practice is to combine HIP and extrusion processing to provide the most uniform powder superalloys for subsequent forging. Superalloys are usually extruded from pre-consolidated billet with a extrusion ratio of 3 to 1. The typical extrusion temperature for PM superalloy is between 1313 and 1448K (1040 to 1175°C) [4].

The consolidated PM material has a number of advantages over CW ingot products. Due to the fast cooling rates of PM powder, the composition of consolidated material in uniform with little signs of micro-segregation. The consolidated powder also possesses a fine grain size that may exhibit superplastic behavior, which increases formability and enable close tolerance forgings without cracking. PM alloys are also more homogeneous compared to most conventional CW superalloys [3].

Initial PM superalloy compositions were modifications of existing alloys such as IN-100 and René 95. These alloys have been used in aircraft engines for more than 20 years and are still widely used. With segregation minimized, alloy designers were able to develop a number of new PM alloys with exceptionally high strength. Current PM alloys, such as René 88DT in this case, have been developed with a focus on increasing defect tolerance, the ability of a material to resist the growth of cracks initiated by a defect in the microstructure.

2.3 Isothermal Forging

After consolidation, the extruded billets of PM Ni-superalloys are cut into mults of specific size and weight. These cylindrical blanks undergo thermomechanical treatments starting with isothermal forging. The isothermal press

forging process forms the mults into the final complex disk shapes. Temperatures and strain rates are selected to promote superplastic behavior during forging because of (1) the high strain that can be obtained without cracking and (2) the low stresses needed during superplastic deformation. This section will review the mechanisms behind superplasticity and its effects on PM superalloy microstructure. Other phenomena that can occur during isothermal forging such as recrystallization and grain growth are also discussed.

2.3.1 Superplasticity

Superplasticity is the capability of certain polycrystalline materials to undergo extensive tensile plastic deformation to high elongation, often without the formation of a neck, prior to failure. Superplastic metals exhibit high values of strain-rate-sensitivity, defined as *m*:

$$\sigma = K\dot{\varepsilon}^m \qquad [2\text{-}1]$$

Where σ is the true flow stress, $\dot{\varepsilon}$ is the true strain rate, and *K* is a constant [5]. Most normal alloys exhibit $m < 0.2$ whereas superplastic alloys exhibit values of $m > 0.4$ [6]. The strain-rate-sensitivity exponent is sensitive to both temperature and grain size; *m* increases and flow stress decreases with increasing temperature and decreasing grain size. Superplasticity is exhibited in most materials above approximately half the melting point and over a specific range of grain sizes and strain rates, usually from 10^{-2} to 10^{-4} /s.

Commonly, superplastic deformation is favorable for alloys with smaller average grain size. Disk alloys such as René 88DT have grain sizes favorable for superplasticity. In these alloys, large volume fraction of secondary phases (30 to

50%) with approximately equal grain size as the matrix is needed to stabilize the grain size. In contrast to traditional recovery-controlled deformation where high dislocation density is observed, superplastic deforming grains remain equiaxed [5]. Transmission electron microscopy studies have shown only limited evidence for dislocation activity within the grains during superplastic deformation. It has been clear for some time that the principal deformation mechanisms in superplasticity are grain boundary sliding and grain rotation. However, the details of the mechanism are still not clear; studies have reported the sliding of groups of grains as a unit while other studies showed that most grain boundaries appear to slide individually and not necessarily at the same time [6-8].

The theory developed by Ashby and Verrall describes a grain-switching event illustrated by Figure 2.1, which schematically shows how superplasticity might occur on the microstructural level [9]. Ashby and Verrall proposed that two processes operate during superplastic deformation, where the microstructure accommodates the imposed strain without accumulating dislocation within grains. First, GBS occurs along with material transport by grain boundary and bulk diffusion to maintain grain continuity. Second, dislocation glide and climb occur at the grain boundaries but makes smaller contribution as the strain rate is reduced.

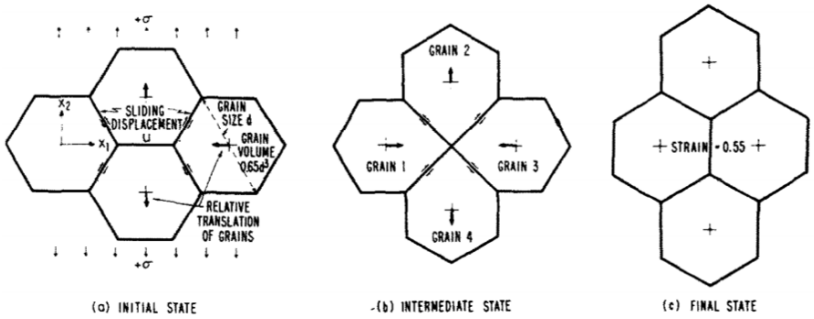

Figure 2.1: Illustration of grain switching event during superplastic deformation [10].

The important characteristics of this model includes the following [10-12]:

1. The ln σ / ln $\dot{\varepsilon}$ curve is sigmoidal.
2. In region I and most of region II there is no large grain elongation or substantial dislocation motion/cell formation. There is however, extensive GBS and grain rotation.
3. At the high strain rate end of region II, dislocation motion becomes important and contributes to both the total strain and accommodation process. The effects of GBS and grain rotation are reduced.
4. In region III dislocation creep is dominant. GBS contributes less and grains elongate.

Ball and Hutchison proposed that, in region II, groups of grains could slide as a unit until an unfavorably oriented grain obstructs them [10]. The resultant stress concentration is released by dislocation motion in the blocking grain, which pile up until the back stress stops the source and therefore the sliding process. Continuation of sliding requires climb by the leading dislocation into and along the boundary, so that further sliding occur at a rate governed by the kinetics of grain boundary climb and dislocations toward annihilation sites. This model predicted the following for region II:

1. A highly strain rate sensitive stress with maximum $m = 0.5$
2. No large grain elongation; extensive GBS and grain rotation. Significant dislocation motion throughout the grain

The structural prerequisites for grain boundary sliding have been well established for metallic, fine-grained materials; several of which have already been

mentioned [5]. First of all, the presence of a second phase is important because grain growth in single-phase materials occurs too rapidly at temperatures where grain boundary sliding occurs. Therefore, second phases are needed to stabilize grain size. Secondly, evidence suggests that the relative strengths of the matrix and grain boundary pinning phase are important in preventing cavitations during superplastic flow; large differences in strength between matrix and second phases induce cavities in many aluminum- and copper-based alloys during superplastic deformation. Thirdly, the grain boundaries between adjacent grains should be high angle (i.e. disordered); low-angle boundaries do not readily slide under the appropriate shearing stresses. The mobility of grain boundaries is also important. During grain boundary sliding, stress concentrations develop at triple points, as well as at other obstructions along the grain boundary. The ability of grain boundaries to migrate during grain boundary sliding permits reduction of these stress concentrations, therefore allowing grain boundary sliding to continue as the major deformation process. Lastly, the grain shape should be equiaxed in order for the grain boundaries to experience shear stress to allow grain boundary sliding. The fact that grains remain equiaxed after extensive superplastic deformation is actually indirect evidence that grain boundary migration is occurring. During GBS, individual grain rotation can reach 20^{o}, while average grain rotation is 5-7^{o} regardless of total strain [13]. The rate of superplastic deformation is related to strain rate, grain size, temperature, and stress [14]:

$$\dot{\varepsilon} = A\frac{F_{gb}\delta G b}{kT}\left[\frac{b}{d}\right]^2\left[\frac{\sigma}{G}\right]^2 \qquad [2\text{-}2]$$

where A is a material constant, F_{gb} is the grain boundary diffusion coefficient, δ is the grain boundary width, b is the Burgers vector, G is the shear modulus, d is the average grain diameter, k is the Boltzman constant, and T is the temperature.

Though there is an abundance of models on superplastic deformation, detailed microstructural studies on superplastic Ni-superalloys deforming under superplastic conditions are limited. There is a lack of understanding of superplastic Ni-superalloy deformation, the effects on microstructure, and its consequences on grain growth during and after deformation. Furthermore, deformation-enhanced grain growth during superplastic deformation, which will be discussed in the next section, has been observed in many alloys [15-17], but there are still disagreements on the mechanisms by which this occurs. Since inhibition of grain growth is important to maintaining superplastic flow as well as in establishing the final grain size during heat treatment, it is important to examine the current theories on grain growth.

2.3.2 Grain Growth

Grain growth in metals is usually understood as the time and temperature dependent increase of the grain size of a single- or multi-phase material. An increase in the average grain size in a constant volume of material is thus connected to the disappearance of some grains, usually the smaller ones. Carpenter and Elam [18] were the earliest to carry out experimental observations of grain growth in 1920. Their conclusions concerning mechanism of grain growth are as follow:

1. Grain growth occurs by grain boundary migration, and not by coalescence of neighboring grains.
2. Boundary migration is discontinuous as a function of time.

3. A given grain can be growing on one side while being consumed by another grain on another side.
4. Consumption of a given grain is more rapid as the grain is about to disappear.
5. A curved grain boundary migrates toward its center of curvature.

Other experimental investigations conducted after those of Carpenter and Elam validated their conclusions [19]. One usually distinguishes between "normal" or "continuous" grain growth and "abnormal" or "discontinuous" grain growth. Hillert [20] states that during normal grain growth, the size of the individual grains are relatively uniform, as contrasted to abnormal grain growth where the differences in individual grain sizes increase as a result of a population of rapidly growing grains.

2.3.2.1 Normal Grain Growth

The theory of normal grain growth kinetics is based on grain boundary interfacial free energy being the driving force, and was first treated by Burke and Turnbull [21] who assumed that the rate of boundary motion is proportional to the curvature of the boundary and that boundary motion is toward center of curvature, as noted by Sutoki [19]. Burke and Turnbull assumed that the driving pressure, P, on a grain boundary arises from curvature, $\kappa = (1/R_1 + 1/R_2)$ of that boundary with principle radii R_1 and R_2. Therefore, for spherical equiaxed grains where $R = R_1 = R_2$, the driving pressure of the grain boundary of energy γ becomes:

$$P = \gamma\kappa = \frac{2\gamma}{R} \qquad [2\text{-}3]$$

By assuming that 1) the radius of curvature, R, is proportional to the mean radius, $\overline{R}$, of an individual grain, 2) the grain boundary energy is the same for all boundaries, and 3) the boundary velocity is proportional to the driving pressure, then:

$$\frac{d\overline{R}}{dt} = \frac{C\gamma}{\overline{R}} \qquad [2\text{-}4]$$

Integrating, we find that the average grain radius is:

$$\overline{R}^2 = \overline{R}_o^2 + Ct \qquad [2\text{-}5]$$

Where $\overline{R}_o$ is the mean grain radius at the initial time, and C is the temperature dependent constant, producing the "parabolic growth law" of grain growth.

Feltham [22], Hillert [20] and others developed the mean field theories for grain growth in which a grain is embedded in an environment which represents the averaged effect of the ensemble of grains. Feltham [22] was the first to use a log-normal grain size distribution f, which was found to fit most experimental data.

$$f = \frac{1}{\sqrt{2\pi\sigma^2}}\frac{1}{D}\exp\left[\frac{-(\ln D - \mu)^2}{2\sigma^2}\right] \qquad [2\text{-}6]$$

Where μ is the natural log of the median radius, D is the average grain diameter, and σ is the standard deviation. Feltham used this distribution to derive the velocity term due to a driving force. Hillert [20], on the other hand, proposed an equation for the driving force in which the velocity of each grain is dependent on its ratio with the average grain size:

$$v = \frac{dR}{dt} = \frac{\alpha M\gamma}{R}\left(\frac{R}{\overline{R}} - 1\right) \qquad [2\text{-}7]$$

where M is the mobility of the boundary and all the other terms are the same as in Burke and Turnbull's equation. In Hillert's formation, a grain smaller than the

average grain size shrinks while grains larger than the average grow. Both Feltham and Hillert's formulations predict the mean growth rate of a system by assuming growth occurs solely as the result of the driving force for removal of boundary curvature.

All of the above-mentioned statistical formations of grain growth lead to parabolic grain growth kinetics as found by Burke and Turnbull:

$$\overline{R}^n = \overline{R}_o^{\,n} + C' t \exp\left(-\frac{Q}{kT}\right) \qquad [2\text{-}8]$$

where $n = 2$ in Burke and Turnbull's formation. The grain size distributions produced by the different formations vary slightly from one another, with Hillert distribution giving the worst fit to experimental results.

Recently a number of computer simulation models of normal grain growth have been developed. Most models can be classified as either direct simulation or statistical, where direct simulations can be broken down into deterministic or probabilistic [23]. The majority of deterministic models use an equation of motion for the velocity of each boundary where as the majority of probabilistic simulations use the Monte-Carlo procedure. Monte Carlo simulations of Anderson *et al*. [24] identified the absorption of curvature by boundaries with little curvature as the mechanism by which the growth exponent (n) increases to above 2, as it is in mean field theories. Simulations by Srolovitz *et al.* [25] agreed with Anderson's conclusion and furthermore identified that larger grains with low boundary curvature exhibit random walk growth kinetics while smaller grains with large boundary curvature migrate rapidly toward extinction by following the driving force of curvature. These

computational simulations concluded that grain growth kinetics relies on both curvature directed motion and random walk.

2.3.2.2 Grain Growth Inhibition

For many industrial alloys where grain growth has been studied, the value of n in the parabolic grain growth equation can be between 6 and 10 [26], which deviates from ideal grain growth kinetics. This large deviation is attributed to mechanisms of grain growth inhibition, which may all cause abnormal grain growth. One of the primary mechanisms is pinning of grain boundaries by secondary phases within an alloy matrix.

When grain boundaries move through an alloy with second-phase particles, there is a tendency for the grain boundaries to be pinned by the particles. Zener [27] showed that if the pinning pressure of the particle is equal to the boundary pressure, then grain growth will cease. For a random distribution of spherical particles of uniform size r and a total volume fraction f_v, Zener found that the hypothetical pinning pressure of a particle would be:

$$P_z = \frac{3 f_v \gamma}{2r} \qquad [2\text{-}9]$$

where γ is the grain boundary energy. Equating boundary pressure with pinning pressure and solving for the average particle-limited grain diameter $\overline{D}_{z,\lim}$, we find:

$$\overline{D}_{z,\lim} = \frac{4\alpha r}{3 f_v} \qquad [2\text{-}10]$$

where α is a constant relating the radius of curvature of the boundary, R, to the grain radius, $\overline{R}$, assuming to be 1 by Zener and 2 by Hillert [20, 27].

2.3.2.3 Superplasticity Enhanced Grain Growth

Superplasticity enhanced grain growth (SEGG), also known as deformation induced grain growth is defined as the strain and strain rate dependent enhanced grain growth observed in materials during deformation as compared to grain growth of materials without deformation at the same temperature. SEGG occurs in both single phase and multi-phase materials during superplastic deformation when other mechanisms such as recrystallization do not dominate. This has important consequences on superplastic forming because flow stress increases with grain size; SEGG produces strain hardening, which in recent studies has shown to be able to retard neck development in tensile tests, thus compensating for the effect of decreasing strain-rate sensitivity as the strain rate decreases [28].

Two models for SEGG have been developed. Clark and Alden [15] proposed that grain boundary diffusivity is increased by grain boundary sliding (the dominant mechanism associated with superplastic deformation) through the production of excess vacancies at the grain boundaries. Since grain boundary diffusivity (D_{GB}) is proportional to vacancy content in the boundaries such that:

$$D_{GB} = C_v D_v \qquad [2\text{-}11]$$

where C_v is the vacancy concentration and D_v is the vacancy diffusivity, excess vacancies increase the grain boundary mobility. The concentration of the excess vacancies, C_E can be expressed by the relationship:

$$C_E = K_1 \tau \dot{\varepsilon} \cdot \left[1 - e^{\frac{-t}{\tau}}\right] \qquad [2\text{-}12]$$

where K_1 is a constant proportional to the vacancy production rate, τ is the vacancy relaxation time, and t is the deformation time. Since vacancies have an equilibrium concentration at any given temperature defined as C_t, the total vacancy concentration

in the grain boundaries is $C_v = C_t + C_E$. The grain growth rate predicted from this model is therefore [29]:

$$\dot{d} = \frac{D_{GB}}{kT}\left(\frac{2\gamma\Omega}{d\delta}\right)^{p} = \frac{K_3\left(C_t + C_E\right)}{d^{p}} \qquad [2\text{-}13]$$

Wilkinson and Caceres [30] proposed a model for SEGG based on the hypothesis that grain boundary sliding induces damage at triple points that is relieved by grain boundary migration in such a fashion as to cause grain growth. This model is also similar to the particle agglomeration model as postulated by Holm *et al.* [16] in which second phase particles agglomerate during superplastic deformation, reducing the number of pinning particles, therefore inducing grain growth. The particle agglomeration model applies to materials where the second phase pinning particles are much smaller than the primary phase grains, which is not the case in Ni-superalloys, where the grain size stabilizing phase (γ') is on the same order of size as that of the primary phase. Therefore, the triple point – lattice damage model is more applicable to the present problem. The grain growth rate predicted by the "lattice damage" model is [29]:

$$\dot{d} = \frac{A_t}{d^{p}} + \frac{\left(\lambda_d d\dot{\varepsilon}\right)\dot{d}_u}{\lambda_d d\dot{\varepsilon} + \dot{d}_u} \qquad [2\text{-}14]$$

where $A_t = \frac{D_{GB}}{kT}\left(\frac{2\gamma\Omega}{d\delta}\right)^{p}$, λ_d is a mechanistic constant of order unity, and $\dot{d}_u$ is the upper limit of the deformation enhanced component of the grain growth rate.

While both of the models above fit to experimental data used by the modelers, it is still yet to be determined which model will describe the grain growth behavior being studied in this research project.

2.3.2.4 Abnormal Grain Growth

Hillert [20] stated that abnormal grain growth could develop in a material if three conditions are simultaneously fulfilled. 1) Normal grain growth cannot take place due to the presence of second-phase particles, 2) The average grain size has a value below $1/2z$, in which z is defined as:

$$z = \frac{3f}{4r} \qquad [2\text{-}15]$$

where f and r are the volume fraction and radius of second phase particles respectively, and 3) there is at least one grain much larger than the average.

Humphreys [31] developed a similar theory defining abnormal grain growth of material with Zener pinning secondary particles. By defining grain growth rate as:

$$\frac{dR}{dt} = \frac{M\bar{\gamma}}{\bar{R}} - \frac{M\gamma}{R} - MP_z = M\left(\frac{\bar{\gamma}}{\bar{R}} - \frac{\gamma}{R} - \frac{3F_v\gamma}{d}\right) \qquad [2\text{-}16]$$

where $\bar{\gamma}$ is the mean boundary energy and $\bar{R}$ is the mean radius, and then replacing the particle pinning term by a dimensionless parameter,

$$Z = \frac{\bar{P}_z\bar{R}}{\bar{\gamma}} = \frac{3F_v\bar{R}}{d} \qquad [2\text{-}17]$$

we get:

$$\frac{dR}{dt} = M\left(\frac{\bar{\gamma}}{\bar{R}} - \frac{\gamma}{R} - \frac{Z\gamma}{\bar{R}}\right) \qquad [2\text{-}18]$$

In this formulation, the condition for instability, leading to abnormal or discontinuous grain growth of a particular grain is:

$$\bar{R}\frac{dR}{dt} - R\frac{d\bar{R}}{dt} > 0 \qquad [2\text{-}19]$$

By expressing the size and boundary parameters of a particular grain in terms of the mean grains as:

$$X = \frac{R}{\overline{R}},\ Q = \frac{M}{\overline{M}},\ G = \frac{\gamma}{\overline{\gamma}} \qquad [2\text{-}20]$$

the instability condition of grain growth then becomes $Y > 0$, where

$$Y = (4Z - 1)X^2 + 4Q(1 - GZ)X - 4QG \qquad [2\text{-}21]$$

The roots obtained by setting Y=0 and solving for X results in two roots that define the bounds of stable/unstable growth. The lower bound X_{min} is the size ratio of the smallest grain or subgrain that can grow abnormally, and the upper bound X_{max} is the maximum value that this ratio can achieve. Figure 2.2 shows the bounds of abnormal grain growth for an ideal grain assembly where all boundary energies and mobilities are equal and the grain misorientation is assumed to be 5°.

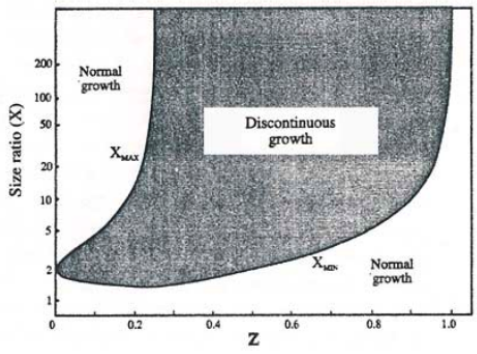

Figure 2.2: Theoretical region of abnormal grain growth with mean misorientation angle of 5 degrees.

Figure 2.3 shows the effects of misorientation on grain growth if the relationship between boundary energy (γ) and misorientation (θ) is:

$$\gamma = \gamma_m \frac{\theta}{\theta_m}\left(1 - \ln\frac{\theta}{\theta_m}\right) \qquad [2\text{-}22]$$

where γ_m and θ_m are the boundary energy and misorientation when the boundary becomes a high angle boundary and the values of boundary mobility (M) are estimated as:

$$M = M_m\left[1 - e^{-b}\left(\frac{\theta}{\theta_m}\right)^n\right] \qquad [2\text{-}23]$$

where M_m is the mobility of a high angle boundary, and n = 4 and B = 5. It is important to note that analyses like that of Humphreys' use an initial log-normal grain size distribution to produce a resultant pinned, narrow grain size distribution, do not produce AGG unless the initial grain size distribution consists of grains that are 10-100x the average grain size.

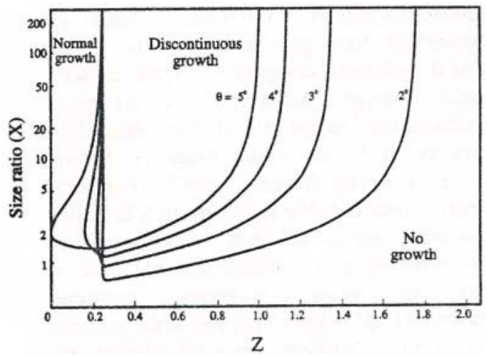

Figure 2.3: Theoretical regions of abnormal grain growth with variations in Z and mean misorientation angle.

2.3.3 Static Recrystallization

In primary recrystallization, a population of new grains is nucleated, often at the grain boundaries of a deformed material, and then grows at the expense of the deformed material until it is all consumed. Nucleation in recrystallization is usually defined as the formation and migration of high angle grain boundaries driven by the stored energy of deformation. Thereafter, grain boundaries continue to migrate, in the form of grain growth, but more slowly. Boundary migration of recrystallized grains is

usually at a uniform rate, producing grains of roughly uniform size. There are 8 major characteristics of recrystallization [21]:

1. Some minimum critical strain is necessary to initiate recrystallization.
2. The smaller the degree of deformation, the higher is the temperature required for recrystallization.
3. Increasing the annealing time decreases the temperature required for recrystallization.
4. The final grain size depends chiefly on the quantity of strain and to a lesser degree the annealing temperature; normally being smaller the greater the amount of strain and the lower the annealing temperature.
5. The larger the original grain size, the greater the amount of deformation required to give equivalent recrystallization temperature and time.
6. The amount of deformation required giving equivalent deformation hardening increases with increasing temperature of working.
7. New grains do not grow into deformed grains of identical orientation, or into grains close to a twin orientation.
8. Recrystallization is slowed if the temperature of deformation is raised while leaving the pre-strain the same, but is accelerated if, at the higher temperature, the metal is strained to the same stress.

The final grain size of the recrystallized material depends on the balance between the nucleation and growth rates; the nucleation rate increases with increased work hardening, but the growth rate increases faster with rising temperature, hence

the 4th characteristic of recrystallization above. The volume fraction of recrystallized grains is usually expressed in the form of [32]:

$$X_v = 1 - \exp\left(-Bt^k\right) \qquad [2\text{-}24]$$

where X_v is the volume fraction recrystallized, t is the time and B and k are material constants. The exact values of the constants vary with material and circumstances. Figure 4 shows typical recrystallization kinetics for isothermal recrystallization.

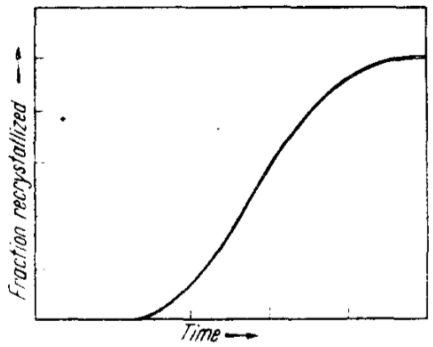

Figure 2.4: Isothermal recrystallization kinetics showing fraction recrystallized as a function of time [21].

Some kinetic experiments have indicated that nucleation rate is low at first and increases to a maximum level, while others show a constant nucleation rate, or immediate nucleation at zero annealing time. Most recrystallization studies indicate that the mechanism of nucleation is intimately linked with the structure of the deformed material, specifically with the degree of misorientation within each deformed grain [20, 32, 33]; nuclei form preferentially in regions where local degree of deformation is highest, such as high angle grain boundaries, deformation bands, inclusions, twin intersections and free surfaces for most metals. From this type of nucleation arose the idea that the orientations of these nucleated grains are present in the previous deformed state [34].

2.3.4 Dynamic Recrystallization

Dynamic recrystallization is defined as recrystallization during hot working or deformation. The flow curves associated with dynamic recrystallization can be cyclic or "single peak". It has been shown that cyclic deformation indicates that grain coarsening is taking place, where coarsening ends when the cycles start to dampen out, while single peak flow is associated with grain refinement [35]. During dynamic recrystallization, nuclei grow rapidly at first, but the concurrent deformation increases the dislocation density with the grains decreasing the driving force for boundary migration; the new grains reach a limiting size and then stop growing, triggering a new cycle of nucleation and growth. Physical mechanisms responsible for dynamic recrystallization are similar to those controlling static recrystallization. The first formal theory of dynamic recrystallization was published by Sandstrom and Lagneborg in 1975 [36]. In their work, the average dislocation density within grains, ρ, determine flow stress by employing the principle that dislocation densities drop to very low values just behind the moving boundaries and then increase linearly with strain. Nucleation occurs when ρ attains a critical value. Though simple, the Sandstrom and Lagneborg model permits the evaluation of the average dislocation density under crystallization conditions, and leads to theoretical stress-strain curves of a periodic nature.

Roberts *et al.* examined the kinetics of dynamic recrystallization in detail [35]. They took grain size changes into account by limited themselves to the case of grain refinement and single peak flow during dynamic recrystallization. In their model, recrystallization occurs at the grain boundaries of pre-existing grains and continues until all nucleation sites are saturated. Once recrystallized grains stop growing due to

impingement of grain boundaries, fresh nucleation events occur at newly created grain boundaries. The layer-wise progression of dynamic recrystallization led to the following expression for the volume fraction of dynamically recrystallized material *X(t)* [35].

$$X = 1 - \exp\left(-2S_v Gt\right) \qquad [2\text{-}25]$$

S_v is the active grain boundary area per unit volume, G is the radial growth velocity, and t is the time. This solution only applies when initial nucleation sites are saturated with recrystallized grains does not apply in the earlier stages of recrystallization when the grain boundary nucleation rate is considered. In order to describe experimental results, the active grain boundary area per unit volume needs to increase with time, therefore yielding the approximate solution below.

$$X = 1 - \exp\left(-\frac{k}{D_o}t^n\right) \qquad [2\text{-}26]$$

Where $n \sim 1.3$ for experimental data, D_o is the initial grain size, k is a material constant that can be considered a fitting parameter in this Avromi equation. Despite the agreement with experimental results, the above solution does not involve the evolution of dislocation density with strain. But since Sandstrom and Lagneborg reported that dislocation density scales linearly with strain [37], the time dependence of equation 2-26 can be exchanged for dislocation density dependence, making the solution more accurate to experimental observations.

Many computer models of dynamic recrystallization involve sequential deformation steps followed by increments of static recrystallization. Recent computer models of dynamic recrystallization suggest that deformation temperature has little

effect on product grain size, whereas deformation stress has a large effect. This is attributed to the increased quantity of nucleation sites at high stress, which causes smaller limiting grain size [38, 39]. The strain-rate dependence of dynamic recrystallization has been receiving more attention recently, but the subject is complex with few general findings [40].

2.4 Heat Treatment

Heat treatment of nickel-based superalloys is critical to overall alloy and component performance. The microstructure produced from isothermal forging operations is not optimal for service applications, therefore the microstructure is manipulated by heat treatments to develop optimum grain size, grain boundary morphology, and phase distributions [41]. Solution treatments are performed on all nickel-based superalloys, except for select materials where direct aging is performed after forging, such as Direct age Alloy 718 [3]. Solution heat treatments are usually performed to dissolve the coarse gamma-prime that result from the forging operation working temperature or the cooling rate from the forging temperature. Solution heat treatments are most often performed just below the γ' solvus, which is 1107^{o}C for René 88DT [42]. Current practice generally utilizes heat treatment temperatures that are supersolvus for René 88DT to fully dissolve γ'. At solution temperatures below the solvus, the presence of γ' precipitates pins grain boundaries, creating a relatively fine grain structure. Supersolvus heat treatments dissolve the γ' precipitates, adding additional grain growth and therefore giving a coarser microstructure.

Equally or potentially more important to the high temperature solution cycle portion of the solution heat treatment is the cooling methods and part cooling rate

profile from the solution cycle. The imposed cooling rate along with the nucleation rates and intrinsic growth kinetics of the precipitating phases produce a morphology and distribution of the secondary phases in the nickel-based superalloys. High cooling rates are required for high volume fraction of very fine γ' and hence high strength [3, 43]. However, cooling rates are limited by the physically large size of turbine disks and complicated by changes in cross sectional thickness.

High temperature solution heat treatment is typically followed by a series of lower temperature heat treatments designed to stabilize the carbide and γ' precipitates. Aging cycles that follow are preformed at temperatures just above the operating temperature, which are too low to contribute significant additional grain growth. These aging cycles improve creep and stress rupture properties of the alloys by allowing carbides and γ' to grow/dissolve/coalesce to equilibrium morphology [43].

2.5 René 88DT Microstructure

René 88DT, a commercial alloy that has been well characterized [2] is a two-phase alloy with small amounts of carbides and borides. The composition of the alloy is shown in Table I.

Table I: René 88DT Alloy composition [1].

Element	Al	Ti	Cr	Co	Zr	Nb	Mo	W	O	C	Ni
Wt %	2.30	3.82	15.14	13.73	0.04	0.71	3.75	3.79	0.01	0.74	Balance

The primary phases of René 88DT are the FCC γ matrix and the γ'(Ni_3Al) ordered precipitates. In the as-extruded state, the two primary phases make up the 99% of the volume in approximately equal fractions. The different alloying elements seen in Table 1.1 partition to the two primary phases such that Cr, Fe, Co, Ni, and Re

partition to the γ matrix in solid solution and the Al, Ti, Nb, and Ta elements partition to the γ' precipitates in solid solution. The γ' precipitates exist in the alloy in three different populations: primary, secondary, and tertiary, the majority of the γ' exists as primary precipitates during forging. Figure 2.5 is a SEM of the as-extruded René 88DT with preferential etching of γ' showing the structure of the primary γ' precipitates.

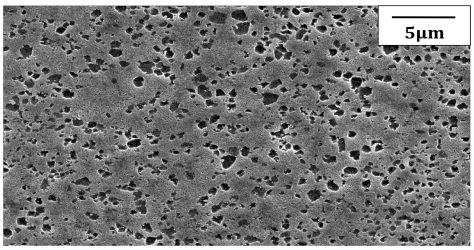

Figure 2.5: as-extruded René 88DT microstructure with preferential etching of γ'.

The microstructure of René 88DT evolves significantly through the thermo-mechanical processing. Figure 2.6 show microstructure of as-extruded, as-forged, and as heat treated and aged René 88DT, respectively. Noting that the scale on each image is different, the microstructure coarsens significantly as the alloy follows through the thermo-mechanical treatments. The focus of this study is the microstructural evolution and deformation responses to forging between the as-extruded and the as-forged states.

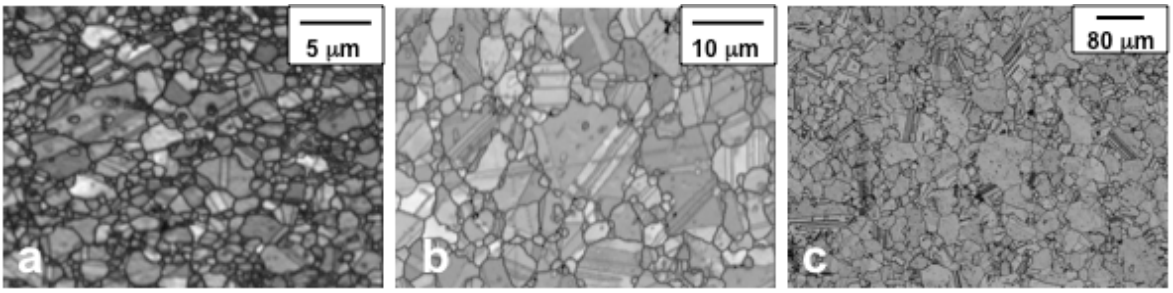

Figure 2.6: microstructure of René 88DT (a) as-extruded (b) as-forged (c) as heat treated and aged.

2.6 Chapter Summary

As shown in the discussion above, much is known about individual thermo-mechanical phenomena relevant to processing Ni-based turbine disk materials, including superplasticity, grain growth, and recrystallization. But in forging and subsequent steps in the turbine disk production process, all of these phenomena occur, sometimes simultaneously. There is a lack of understanding of how these phenomena interact with each other as a function of temperature, strain, and strain rate during forging. The critical temperature and strain rates that induce each of these microstructural behaviors are also unknown. Understanding and predicting the mechanisms that occur during forging on the grain scale is important in predicting grain behavior during the subsequent steps in the disk production process. Furthermore, there are consequences of each deformation mechanism on the microstructure of the post-forged disk. These are the motivations for this research.

In the subsequent chapters, characterization of microstructure, strain storage, and strain accommodation mechanisms during high temperature deformation of René 88DT at conditions that simulate forging will be presented. Evidence for various deformation mechanisms will be discussed along with the microstructural evolution corresponding to the different deformation mechanisms. The boundaries of different deformation mechanisms, as well as grain structure evolution during deformation will be described using constitutive models.

Chapter 3

Local Strain Distribution on the Super-granular Scale

A high temperature surface displacement mapping technique developed at the University of Michigan has been used to analyze strain accumulation at the grain scale during high temperature deformation. This strain mapping technique, which utilizes physical marker grids on the surface of the sample, analyzes displacement of individual surface markers to measure local accumulated strain. The individual markers are identified by an IDL (Interactive Data Language) program, which uses grayscales to distinguish differences between markers and sample surface in SEM images [44]. Pre and post-deformation SEM images of the marker grid are subjected to digital image correlation algorithms in an IDL program to create strain maps of the image area. It has been shown that the surface strains measured using strain mapping are representative of the deformation experienced by the bulk for simple monotonic loading [45]. Using data collected from the strain maps, strain distributions can be correlated with microstructural features. Microstructural scale strain distributions provide information on the uniformity of strain accumulated within the sample, and the role of specific microstructural features.

3.1 Surface Strain Mapping Experimental Procedure

3.1.1 Sample Fabrication

The strain mapping procedure starts with sample fabrication. For this study, samples were cut out of a powder-extruded billet of René 88DT using wire electrical discharge machining (EDM). The cut strain mapping samples were rectangles with dimensions of 5mm in width by 5mm in depth by 10mm in height. Once cut, the sample surfaces perpendicular to the compression direction were grooved with a X-shape of 0.5mm depth to retain lubricants during compression. Furthermore, every sample edge in contact with compression platens during compression was rounded using 320μm silica carbide grinding paper. One sample surface parallel to the compression direction was then polished using 320-400-600-1200 grit silica carbide grinding papers, followed by 6-3-1μm diamond polishing solutions.

3.1.2 Grid Deposition and Marker Identification

In the strain mapping procedure, Pt markers are first deposited on a polished surface of a compression sample by sputter coating through a 2000 lines/in. nickel mesh screen affixed to the surface. Pt was chosen over other marker materials such as Au or Au/Pd because of its high melting temperature and lower oxidation tendencies at forging temperatures. To ensure sharp contrast of Pt markers under back-scattered mode in the SEM, the target marker thickness during sputter coating was optimized at 0.5μm.

After deposition of the Pt markers and the removal of the nickel mesh, the sample was imaged in a Philips XL30 FEG SEM in the back-scattered electron (BSE) mode. Figure 3.1 shows a typical Pt gridded sample surface before compression.

During sequential straining steps, it is important to be able to return to grid points within the same region, so great care is taken to make sure that the same location of the sample can be identified after compression and the measured displacement of the markers are not skewed by rotation of the sample. After compression testing, the samples are imaged again to measure marker displacements. The pre- and post-deformation SEM images are processed in the IDL code to obtain displacements and corresponding strain mapping data.

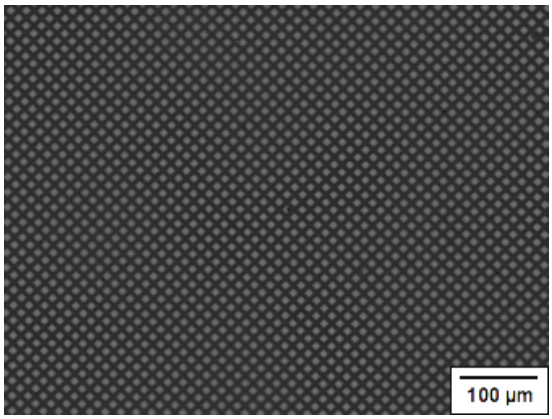

Figure 3.1: Sample surface Pt grid markers before compression.

There are limitations to the magnitude of strain that can be mapped using this technique. Marker identification and matching becomes less reliable at accumulated strains beyond 0.1 due to marker movement. Therefore map strain accumulation at higher strains samples had to be pre-deformed before Pt grids were applied; samples were deformed to 0.3 and 0.5 strain before marker deposition, compression, and mapping. Strain accumulation can be studied at higher imposed strains using this method though total strain accommodation is not recorded.

3.1.3 Compression Testing for Strain Mapping

After deposition and imaging, samples undergo compression testing in an Instron® 5582 system at elevated temperatures. To prevent oxidation of the marker-

deposited surface, the sample is covered by tantalum foil and enclosed in a quartz tube with a strong flow of argon gas. Induction heating is used to bring the sample to the desired temperature at a rate similar to that of figure 3.2. Once the compression test is completed, the induction heating system is immediately turned off and the sample is allowed to cool in the quartz tube with the flow of argon gas. The compression test set-up is shown in its entirety in figure 3.3.

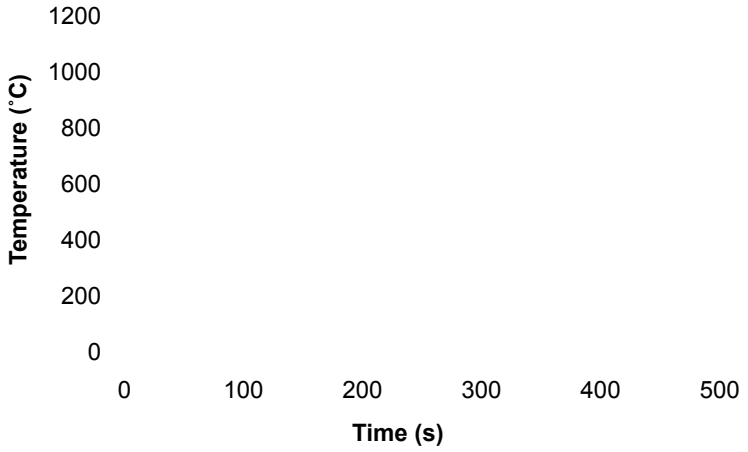

Figure 3.2: Induction heating profile sample for compression tests with 4mm diameter 7mm height sample.

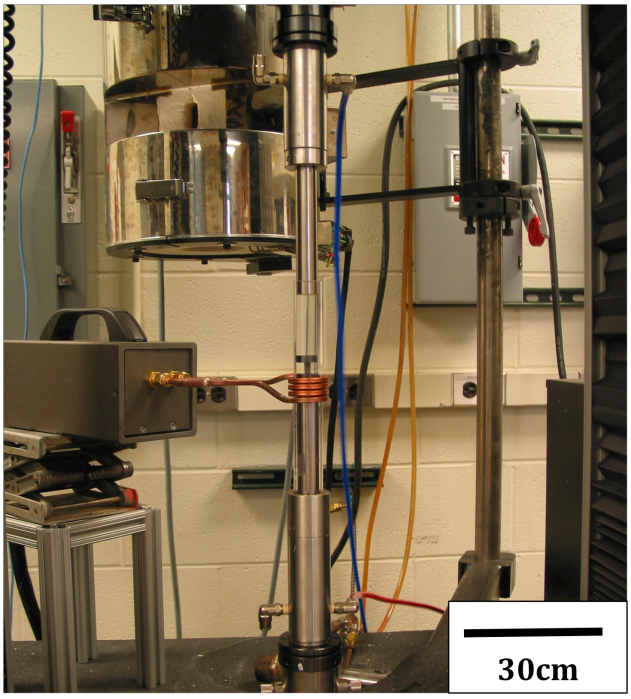

Figure 3.3: Compression Set-up.

3.2 Experimental Results

Surface strain mapping experiments have been conducted on as-extruded René 88DT at 4 different strain rates (0.00032, 0.0032, 0.032, 0.1/s) to 3 different engineering strain levels (0.1, 0.3, 0.5). Figure 3.4 shows a surface strain map of a sample compressed to 0.1 strain at a 0.00032/s strain rate. The map illustrates the distribution of Von Mises strain using a color gradient to represent different levels of strain locally. The vertical axis of the map represents the compression direction. The map shows strains in the range of 1.4 – 0.6 times the nominal strain, where dark orange and blue areas indicate local areas of high and low strain, respectively.

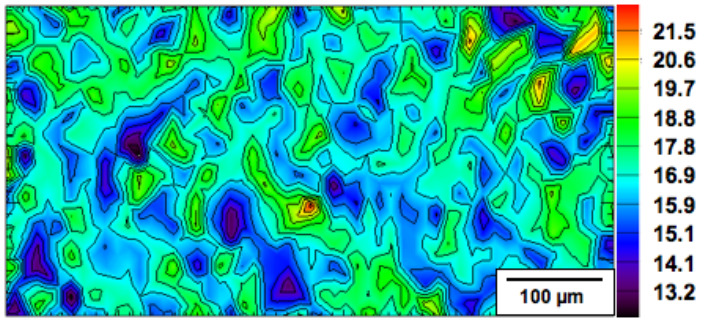

Figure 3.4: Von Mises strain map for sample compressed at 0.00032/s to 14.5% strain. Scale bar in percent Von Mises strain.

Closer analysis of sample surface with SEM imaging in the Backscatter Electron (BSE) mode shows highly deformed grains surrounding large grains with low accumulated strain compared to the imposed strain in areas that correlate to strain map areas of high and low strain respectively (Figure 3.5). These non-deforming grains were observed in samples compressed at all strain rates. Large grains are present in René88DT before compression, which leads to the conclusion that the non-deforming large grains are a product of the powder extrusion process and not of the compression testing. Interestingly, electron probe micro-analysis (EPMA) indicates that there were no statistically significant compositional differences in the major

elements in the large grains compared to the nominal René88DT composition. In this case the strain mapping technique is clearly useful for identification of microstructural features that are significant to the deformation process. In Figure 3.5, the SEM image shows that grain boundary offset of the majority of the grains disrupts the regular shape of the markers. However, since only a small amount of strain was accommodated by the large grain in the center, the markers remained intact. The strain maps show that the center-to-center distance between local regions of high strain next to regions of low strain is between 20 and 50μm, which is 1.5 orders of magnitude larger than the average size of the grains but does correspond to the size of the abnormally large grains. However, the strain maps do not exhibit areas of high strain above and below areas of low strain in the compression direction, indicating that the resolution of the strain maps in not enough to resolve strain imposed on the grains surrounding the large grains.

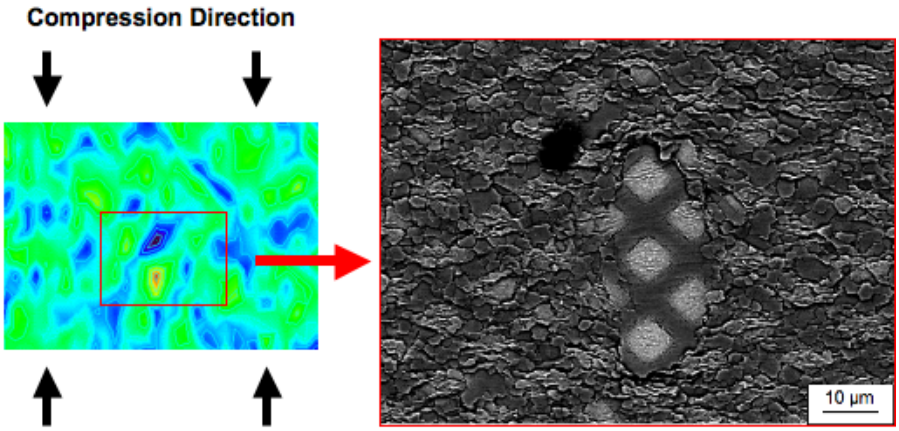

Figure 3.5: BSE SEM image of large grain with low strain surrounded by highly deformed grains after compression on right compared to representative strain map of area around a similar large grain. Compression at 0.001/s strain rate to 0.228 engineering strain.

In Figure 3.5 and 3.6, it is noteworthy that individual grains become visible on the polished surfaces after compression due to the development of large offsets at grain boundaries that occur in samples compressed at the lower two strain rates.

These offsets were not observed in samples compressed at the higher two strain rates. It has been shown that during superplastic deformation, grains may reorient by as much as 15 degrees to accommodate the strain, and this is accompanied by the development of large offsets between grains at the sample surface [10]. Therefore, the transition between low strain rate conditions where the grain offsets develop and high strain rates where they are absent indicates a change in straining mechanism (Figure 3.6), as will be discussed further in chapters 4, 5, 6, and 7.

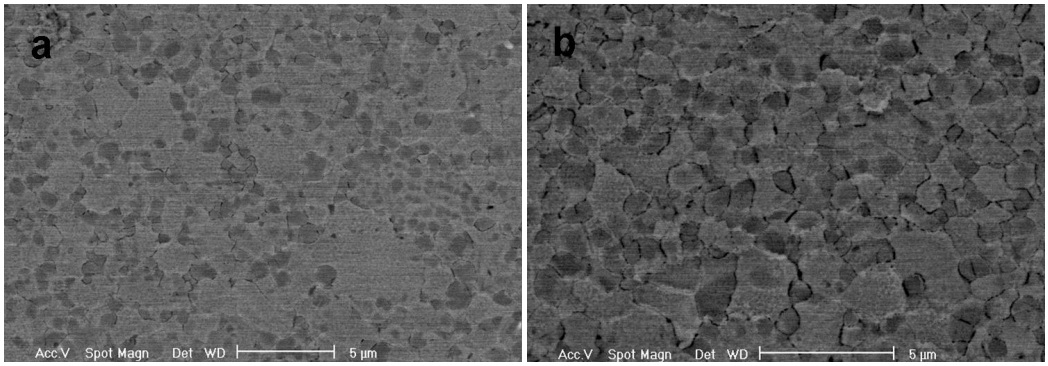

Figure 3.6: Microstructure of strained René88DT shows grain boundary offsets for superplastic deformation. (a) 0.05 strain, 0.032/s. (b) 0.05 strain, 0.0032/s.

Figure 3.7 shows the distribution of strain within samples compressed at 0.00032/s strain rate. The distributions show that the accumulated strain varies between 0.6 to 1.4 times the imposed strain, again indicate that straining occurs inhomogeneously on the micron scale (considering the 12.7μm spacing between center of neighboring markers). Figure 3.7 illustrates that the majority of strain is in the region of 0.8 – 1.2 times the nominal strain, though localized strain can range from 0.6 to 1.4 times the macroscopically imposed stress, as stated above. The vertical axis of Figure 3.7 is the number of pixels normalized by the number of pixels at the peak of the strain distribution. The full-width half-max (FWHM) of the Von Mises strain distributions are shown in Figure 3.8. The distribution width, i.e., the

variability in the local strains, changes as a function of strain and strain rate. However, the cause of the variability in local strains is not well understood.

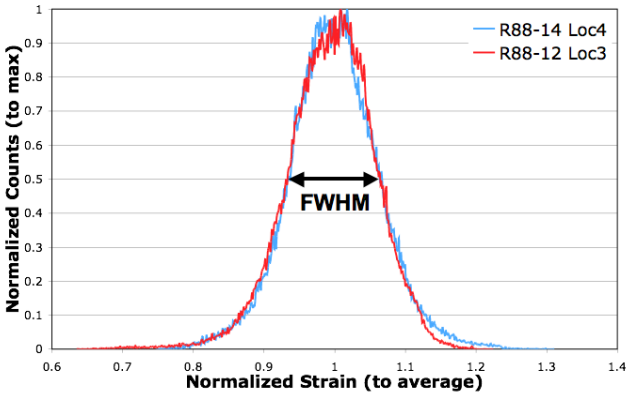

Figure 3.7: Von Mises strain distribution for 0.1 strain at 0.00032/s strain rate. Different colors indicate different samples. Black line with arrows indicates where FWHM is measured.

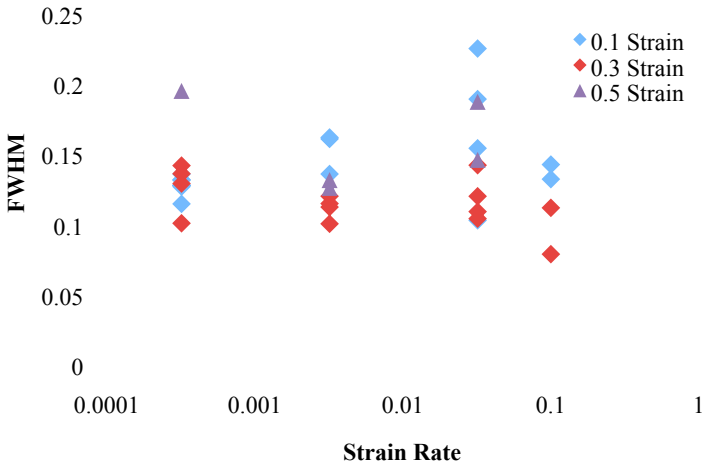

Figure 3.8: Full-width half-max of strain distributions for all René88DT strain maps. Y-axis is width of normalized strain distribution, such as shown in Figure 3.7.

3.2 Discussion and Summary

Strain mapping data has provided quantitative information on strain distribution at the microstructural scale with images that clearly illustrate the non-uniformity of strain accumulation. However, strain mapping is not able to show microstructural evolution during deformation and the dynamic processes that are associated. Therefore, strain mapping can be through of as a way to determine how the microstructure accommodates imposed strain but not how the microstructure

stores the strain. Strain maps are also a useful technique for identifying large non-deforming grains that may serve as crack initiation sites in the René 88DT microstructure. Fatigue studies of Ti-alloys used for turbine and rotors have shown that hard inclusions are likely to be initiation sites for fatigue cracks [46-48]. Strain maps show high strain gradients around areas of irregularly large grains, which indicate that these grains accumulate less strain than the rest of the microstructure. In some cases, the strain increases by 2x from the low strain area to the high strain area. Chemical analysis shows that the large grain has no variability in composition when compared to the rest of the microstructure. It is likely that the large grains are a product of the powder processing of the alloy. Closer analysis of the powder sifting, consolidation, and extrusion processes is needed to understand the cause of these large grains and methods to reduce their frequency.

Despite these results, the utility of strain mapping data in identifying and understanding deformation mechanisms during forging is limited due to the poor resolution of the technique compared to the size of the average grain within the René 88DT microstructure. As noted above, the center-to-center distance between nearest neighbor markers is 12.7μm, which is 6 times larger than the average grain size of the as-extruded René 88DT microstructure. The variation of strain of the majority of the microstructure at this resolution is between 0.8 and 1.2 of the imposed strain, indicating that the variation of strain within groups of grains is narrow at the tested strain rates. However, this does not suggest that variation strain accumulation in individual grains is narrow; as illustrated by the measured strain near large grains, the strain accumulation between grains can vary greatly.

Chapter 4

Flow Stress Evolution During High Temperature Compression

High temperature compression tests are used to simulate high temperature forging of René 88DT. This chapter discusses the experimental methods involved in conducting the compression tests. Furthermore, the response of samples to varying compression temperatures, strain rates, and strain are reported. The final section of this chapter discusses the constitutive flow stress response of the material.

4.1 Experimental Procedures

Cylindrical René 88DT samples with dimensions of 4mm in diameter and 7mm in height are cut from an as-extruded billet using EDM. Once cut, the sample surfaces perpendicular to the compression direction were grooved with a X-shape of 0.5mm depth to retain lubricants during compression. Furthermore, sample edges in contact with compression platens during compression is beveled using 320μm silica carbide grinding paper.

High temperature compression tests are executed in an Instron® 5582 system. Unlike during the strain mapping procedure, oxidation of sample surface is not a concern; therefore, no tantalum foil or quartz tube is used. Induction heating is used to bring the sample to the desired temperature at the same heating rate as that reported

for strain mapping compression tests (see Figure 3.2). Once the desired temperature is reached, the temperature is allowed to equilibrate for 3 minutes before compression begins. Desired strain rate is set as a compressive engineering strain rate, not a true strain rate. Furthermore, the test ends at either an input compression strain or time. Once a compression test is complete, the induction heating system is immediately turned off. At the same time, a cooling fan directed at the sample is turned on to expedite the cooling process. The sample temperature cools to 773°K (500°C) within 10 seconds of completion of compression test. The temperature is measured by an k-type thermocouple attached to the surface of the samples.

4.2 Experimental Results

René 88DT samples were compressed at 4 different temperatures 1323K (1050˚C), 1298K (1025˚C), 1269K (996˚C), 1241K (968˚C) with 4 different imposed strain rates (0.00032, 0.0032, 0.032, 0.1/s). The flow stress of each sample is shown in Figure 4.1 – 4.4. Each figure shows flow stress of samples compressed at specific test temperatures. Though only one stress-strain curve is shown for each strain rate, the compression tests were conducted several times and the stress-strain curves were consistent and reproducible.

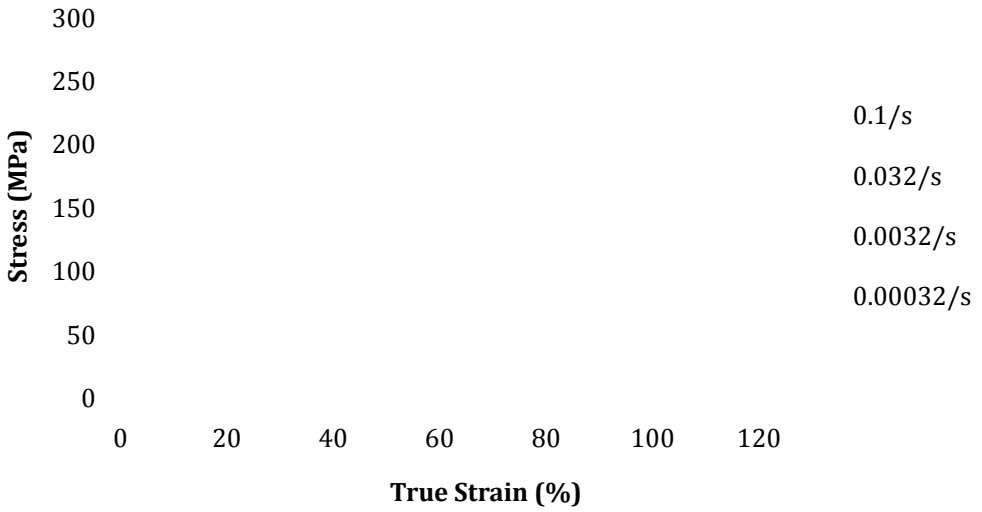

Figure 4.1: True stress strain curves for René 88DT compressed at 4 different strain rates, all at 1241K (968˚C).

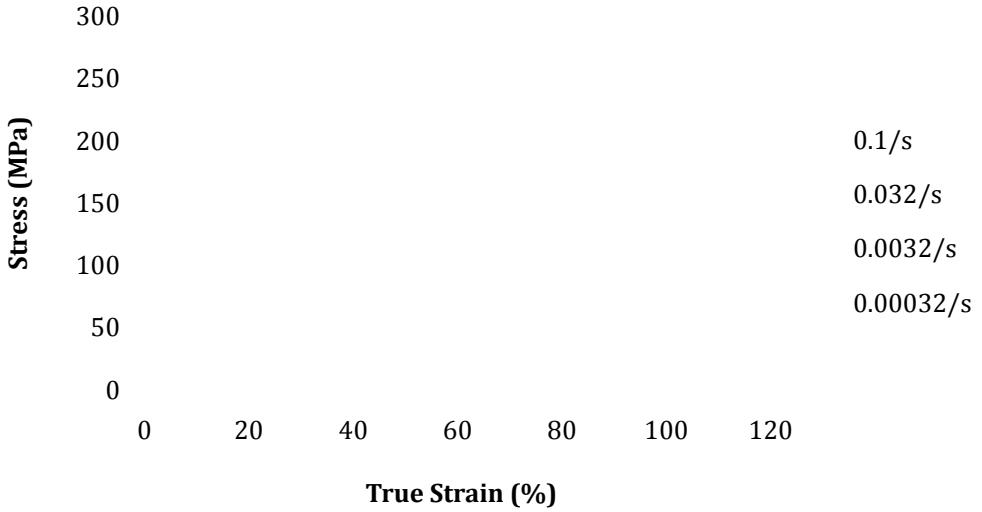

Figure 4.2: True stress strain curves for René 88DT compressed at 4 different strain rates, all at 1269K (996˚C).

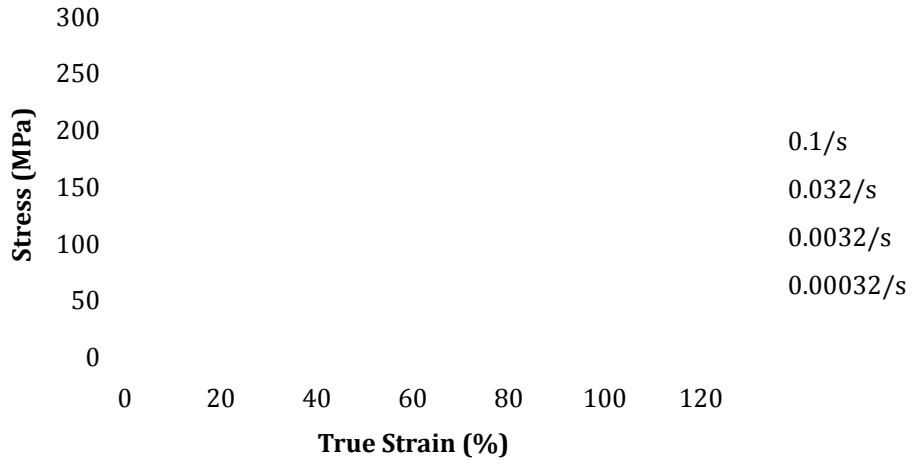

Figure 4.3: True stress strain curves for René 88DT compressed at 4 different strain rates, all at 1298K (1025˚C).

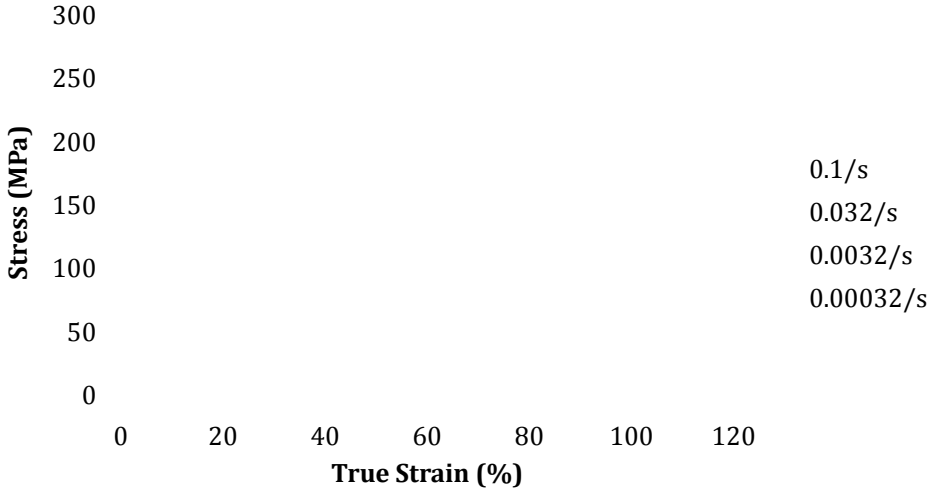

Figure 4.4: True stress strain curves for René 88DT compressed at 4 different strain rates, all at 1323K (1050˚C).

As shown in Figures 4.1-4.4, both the yield strength and flow stress increase with strain rate and temperature. Figure 4.1 shows the stress-strain curves of samples compressed at 1241K (968˚C); at this temperature, René 88DT exhibits significant strain softening at 0.1/sec and 0.032/s strain rate. At the same temperature but a slower strain rate of 0.0032/s, strain softening transitions to strain hardening around 60% true strain. At the slowest strain rate of 0.00032/s, René 88DT exhibits significant strain hardening with no evidence of strain softening at any strain. Figure

4.2 shows the stress-strain curves of René 88DT compressed at 1269K (996˚C). At this intermediate temperature, strain softening is only observed at the highest strain rate of 0.1/s; the flow stress stays relatively constant at 0.032/s and strain hardening is observed at the lowest strain rates (0.0032, 0.00032/s). Figures 4.3 and 4.4 show that at the highest compression test temperatures [1323K (1050˚C), 1298K (1025˚C)], strain hardening is observed at all strain rates. Furthermore, compression at 0.1/sec strain rate shows steady state flow stress before 60% true strain, at which point strain hardening occurs.

Figure 4.5 shows the progression of flow stress evolution of samples compressed at 1298K (1025˚C) with varying strain rates. Strain hardening is exhibited at all strain rates, though strain hardening initiates at a much higher strain when compressed at a high strain rate; strain hardening occurs almost immediately after yield at low strain rates. At higher strain rates, small amount of strain softening occurs after yield, followed by strain hardening at around 60% true strain. The ratio of flow stress at 110% true strain to yield strength increases as strain rate decreases (Figure 4.6) signifying that the magnitude of strain hardening relative to yield stress increases with decreasing strain rate. This is interesting since strain hardening usually increases with increasing strain rate [49-52]. The possible mechanisms responsible for the observed strain hardening are discussed in the discussion section of this chapter.

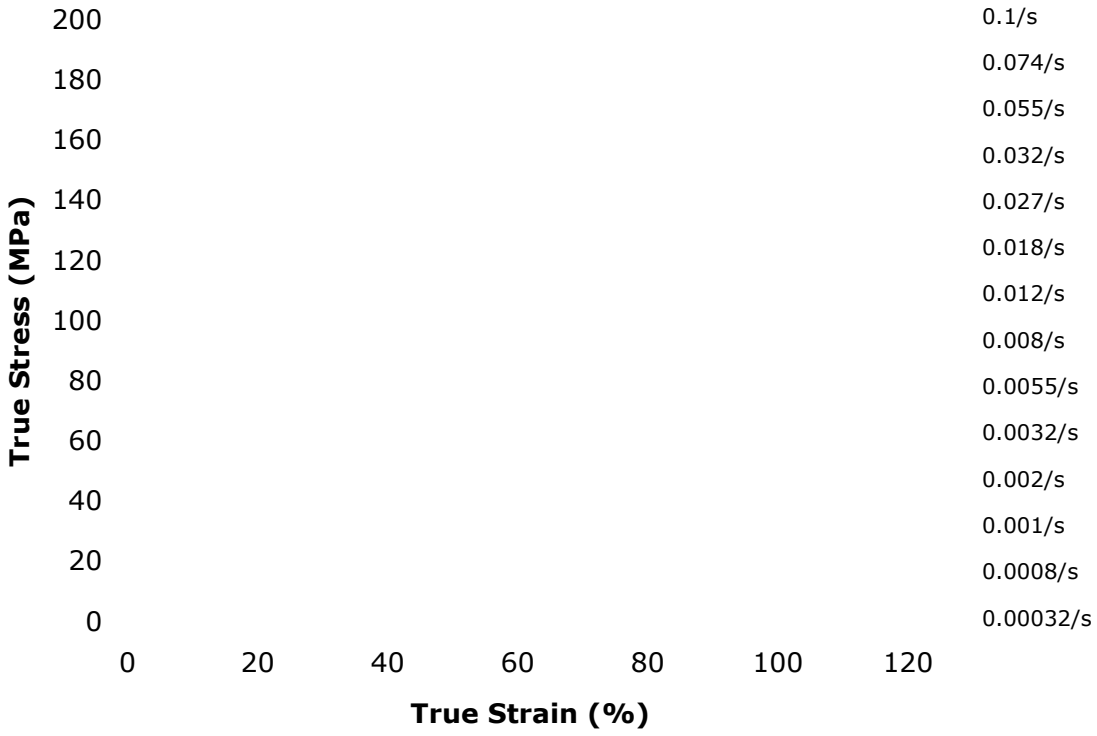

Figure 4.5: True Stress-strain curves for René 88DT compressed at different strain rates all at a temperature of 1298K (1025˚C).

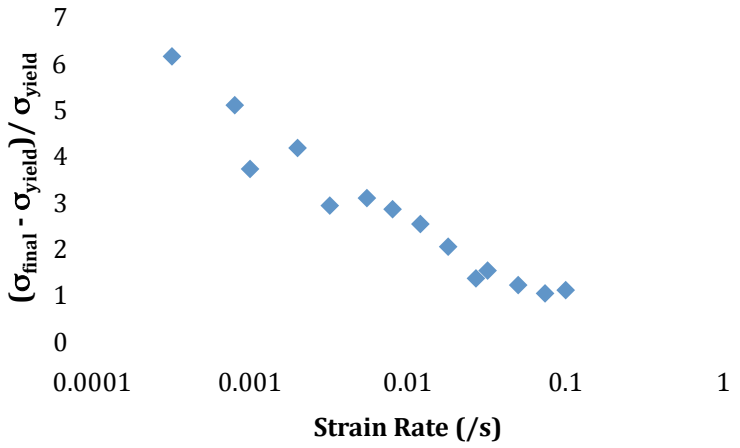

Figure 4.6: Ratio of flow stress at 110% true train to yield stress for René 88DT compressed at different strain rates all at 1298K (1025˚C).

The adiabatic corrected flow stress at 70% true strain is shown in Figure 4.7. The isothermal flow stress at each test temperature was determined at 70% true strain through linear interpolation between adjacent temperatures using the following equations:

$$\Delta T(\varepsilon) = \frac{f}{\rho \cdot C_p} \int_0^{\varepsilon} \sigma d\varepsilon \qquad [4\text{-}1]$$

$$f = \begin{cases} 0 \xrightarrow{when} \dot{\varepsilon} \le 0.001 \\ \dfrac{\log(\dot{\varepsilon})/3+1}{m+1} \xrightarrow{when} 0.001 \le \dot{\varepsilon} \le 1.0 \\ \dfrac{1}{m+1} \xrightarrow{when} 1.0 \le \dot{\varepsilon} \end{cases} \qquad [4\text{-}2]$$

where ρ is the volumetric density, C_p is the specific heat, ε is the true strain, $\dot{\varepsilon}$ is the strain rate, σ is the flow stress, and m = 0.11.

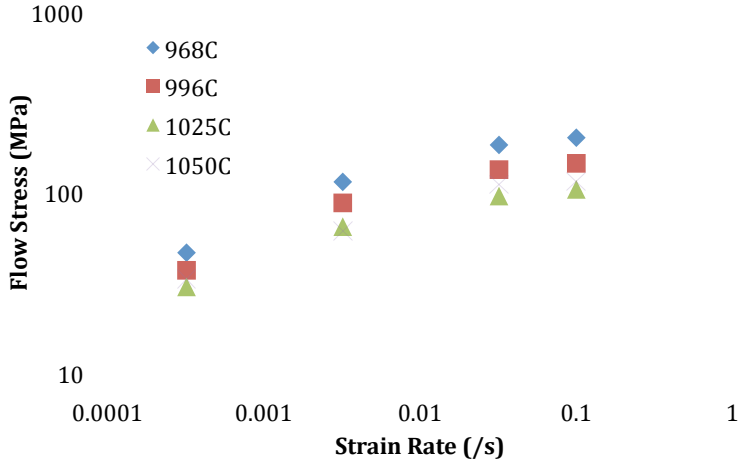

Figure 4.7: Adiabatic flow stress at 70% true strain for René 88DT compressed at different strain rates and temperatures.

4.3 Discussion

Isothermal compression of metallic materials can be described by a relationship between flow stress (σ) and strain rate ($\dot{\varepsilon}$):

$$\sigma = k\dot{\varepsilon}^m \qquad [4\text{-}3]$$

where k is a material constant, and m is the strain rate sensitivity coefficient. The strain rate sensitivity coefficient of René 88DT can be measured for the testing conditions using a log-log plot of stress versus strain rate such as Figure 4.7. The average strain rate sensitivity for test temperatures ranges from 0.11 at the highest

strain rates to 0.52 at the lowest strain rates. As mentioned in the previous chapter, a strain rate sensitivity coefficient of higher than 0.4 is usually associated with superplastic deformation, while a strain rate sensitivity coefficient of below 0.2 is associated with power-law creep deformation. Therefore, the measured strain rate sensitivity coefficient for René 88DT suggest that two different deformation mechanisms are present for the testing conditions; superplastic deformation occurs at low strain rates while power-law creep deformation occurs at higher strain rates. The transition between the two deformation mechanisms is observed by the strain rate sensitivity coefficient evolution to occur between 0.001/s and 0.032/s strain rate. The transition of strain rate sensitivity coefficient also suggests that there is a transition in deformation mechanism that is both strain rate and temperature dependent. Adiabatic heating corrections were applied to the measured flow stresses for all testing conditions. However, finite adiabatic heating was only observed at strain rates of 0.032/s and 0.1/s. Deformation at slower strain rates did not cause measurable changes in the sample temperature.

Strain hardening is observed during compression of René 88DT in the temperature range between 1241K (968˚C) and 1323K (1050˚C), which corresponds to T/T_m of 0.7 – 0.8. Figure 4.6 shows that relative strain hardening increases as strain rate decreases. Mechanisms for strain hardening are usually attributed to the increase in defect substructure during straining. However, the balance of kinetics of dislocation creation and recovery determines the magnitude of strain hardening. Therefore, hardening and softening occur due to changes in the dislocation structure due to enhanced recovery kinetics, recrystallization, and grain growth. Studies have

shown that strain hardening is rate dependent due to the time-dependent process of dislocation recovery such that the magnitude of strain hardening is inversely proportional to the time allowed for recovery processes; during deformation at high strain rates where less time is allowed for recovery to occur, the magnitude of strain hardening increases when compared to deformation at low strain rates [53, 54]. However, flow curves of René 88DT show increasing strain hardening as strain rate decreases within the range of conditions tested. Increasing strain hardening as a function of increasing strain rate during superplastic deformation has been observed in titanium alloys although there has been no discussion of attributing mechanisms [55]. The strain hardening observed at low strain rates can be attributed to the evolution of the grain structure during compression in René 88DT. During superplastic deformation, which occurs at low strain rates, the energy needed for grain boundary sliding is proportional to the square of the grain diameter [56] (see equation 2-2). Therefore, as grains coarsen during compression, the stress increases; because compression time scales inversely with strain rate, samples compressed at the slowest strain rates experience longer times at elevated temperatures, meaning more grain coarsening. The grain coarsening during compression explains the phenomenon of higher relative strain hardening as a function of the yield stress at lower strain rates. The phenomenon of grain coarsening will be discussed in much detail in the next chapters. Strain hardening can also occur during power-law creep deformation when the dislocation density inside grains increases during deformation, causing dislocation entanglement. This type of grain hardening occurs until a critical dislocation density is reached to trigger dynamic recrystallization [32].

Strain softening is observed at the highest strain rates during compression, which is most apparent at the lowest test temperature of 1241K (968˚C). Strain softening is usually attributed to recovery mechanisms such as dislocation annihilation and dynamic recrystallization [34]. During deformation at high strain rates, dislocations do not have the time needed to travel to the grain boundaries, where they are annihilated. Therefore, the most logical explanation for the observed grain softening at high strain rates during compression of René 88DT is the occurrence of dynamic recrystallization. A single wave of dynamic recrystallization during compression corresponds to a single peak flow stress [35], which is observed for René 88DT at higher strain rates at all test temperatures. Dynamic recrystallization will be discussed in detail in the subsequent chapters.

4.4 Chapter Summary

In this chapter, the flow curves of René 88DT during compression were presented for the temperature range of 1241K (968˚C) to 1323K (1050˚C) at strain rates between 0.00032/s and 0.01/s. The flow curves were used to calculate the strain rate sensitivity coefficient at test conditions. The strain rate sensitivity coefficient (m) evolved as a function of strain rate such that high m indicating superplastic deformation was observed at low strain rates and low m was measured at high strain rates indicating an evolution to power-law creep deformation. Counter to generally observed behavior of strain hardening, the flow curves showed decreasing strain hardening as strain rate increased. The high degree of strain hardening at low strain rates is attributed to grain coarsening during superplastic deformation, which in turn increased the energy necessary for grain boundary sliding.

Chapter 5

Microstructural Evolution During High Temperature Compression

In the previous chapter, analysis of the high temperature flow behavior indicated the presence of two different deformation mechanisms during high temperature compression of René 88DT in the temperature range of 1241K (968˚C) and 1323K (1050˚C). The measured strain rate sensitivity coefficient indicates that superplastic deformation dominates at low strain rates and power-law creep deformation occurs at high strain rates. However, the presence of hardening and softening phenomena were observed across the range of experimental conditions investigated. For this reason, it is important not only to measure the material response during deformation, but also to understand the microstructural evolution during deformation. In this chapter, EBSD grain size data is presented and microstructural evolution as a function of temperature, strain, and strain rate during high temperature compression of René 88DT is discussed.

5.1 Experimental Procedure

Grain size evolution and strain storage within René 88DT during compression have been analyzed using Electron Backscatter Diffraction (EBSD), which uses backscattered electron-generated diffraction patterns to measure local

crystallographic orientation in a scanning electron microscope (SEM). During operation of a SEM, some fraction of the incident electrons scatters inelastically from crystallographic planes of the sample. These electrons form a diffraction pattern on the EBSD detector, which is generally a phosphor screen oriented near the sample. The diffraction patterns are called Kikuchi patterns, which are captured by a charged-coupled device (CCD) camera and sent to a computer to be indexed. A simple schematic of an EBSD system is shown in Figure 5.1.

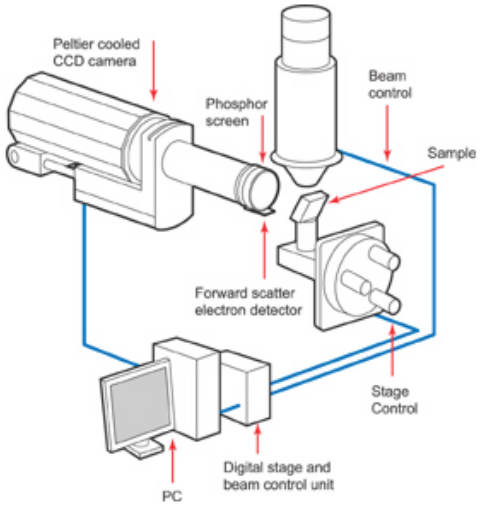

Figure 5.1: Schematic of EBSD system [57].

The indexed Kikuchi patterns define the orientation of the crystal at localized scan spots. Abrupt changes in scan point crystallographic orientation between neighboring points are used to distinguish grain boundaries, therefore allowing for the measurement of grain size. Changes in crystal orientation that occur due to dislocation storage and local strain gradients are also captured and can be analyzed by measuring misorientation within individual grains [58]. Recent investigations on steel and nickel alloys have demonstrated a correlation between stored dislocation density measured by TEM techniques and misorientation maps generated by EBSD [59, 60].

5.1.1 EBSD Sample Preparation

EBSD samples are prepared as follows. Cylindrical compression samples with dimensions of 4mm diameter and 7mm height are cut by wire EDM from an as-extruded billet of René 88DT. All sample edges are then rounded using 320 grit silica carbide grinding paper and sample surfaces perpendicular to compression direction are grooved with a 0.5mm deep X to retain lubricant and reduce bulging during compression. The lubricant used is boron nitride, which is sprayed onto carbide platens in contact with the compression samples.

Once prepared, EBSD samples are compressed in an Instron® 5582 system at elevated temperatures. The same induction heating system that is used during compression of strain mapping samples is used in these experiments. The EBSD samples are not covered with tantalum foil or enclosed in argon filled quartz tube because oxidation is not a concern for EBSD experiments since only subsurface regions are examined. A thermocouple is in contact with samples during compression to ensure accurate experimental temperature. After compression, samples are either air-cooled or water quenched, which will be indicated in experimental results and discussion.

After compression, samples are cut, perpendicular to the compression direction using a low-speed diamond saw, to expose the center of the sample; EBSD scans are taken of the center of this surface. The exposed sample center surface is polished with the same procedure as for strain-mapping samples but with an additional vibratory polishing step; the samples are vibratory polished with a Buehler

Vibromet 2 in colloidal silica polishing suspension for 3-6 hours at 30-40% intensity after mechanical polishing.

5.1.2 EBSD Grain Size Measurement

EBSD scans are taken in a Philips XL30 FEG SEM at 20kV with a predetermined step size. A spot binning of 8x8 and an exposure time of 0.03s on individual scan spots is used during the scans. Once scans are complete, a cleaning algorithm removes all scan points with confidence index below 0.1 and minimum grain size is set to 5 scan points, therefore all grains less than 5 scan points are incorporated into the surrounding grain. Payton *et al.* determined in a statistical analysis that majority of grains less than 5 scan points at a scan step size of 0.2μm are artificial grains as a result of small areas of poor indexing by the orientation imaging software [42].

Once an EBSD scan is compete, grains can be defined by the degree of misorientation between scan points such that a grain boundary is defined between scan points of more than 5 degrees of misorientation. Once the grain boundaries are defined, the area of each grain can be determined by determining the number of scan points within an enclosed boundary. This area data can then be converted to ASTM grain size, linear intercept grain diameter, and also stereologically corrected grain diameter using the ASTM E112. Reported grain diameters are the linear intercept grain diameters. One has to keep in mind that the orientation imaging software cannot distinguish between γ and γ' phases and as a consequence all incoherent γ' phase particles larger than the defined grain criteria mentioned above (5 scan points) are considered individual grains. On the other hand, all coherent γ' are incorporated into

the parent γ grain, therefore artificially making the grain larger. All EBSD scans were completed on an area of 40μm by 40μm on each sample. EBSD measured about 1000 grains in such a scan area for the as-extruded sample. The number of grains counted by EBSD was between 400 and 1500 for samples after deformation at different conditions. This sampling size is assumed to be large enough to make grain size and other grain structure average properties statistically relevant.

5.2 Microstructural Evolution during Thermal Transients

Before high temperature compression tests were conducted, evolution of microstructure during pre-deformation heat-up and hold step was observed. Four samples were heated to target temperatures of 1323K (1050˚C), 1298K (1025˚C), 1269K (996˚C), 1241K (968˚C) and held using the same temperature profile as compression samples. Once heating was complete, samples were air cooled to room temperature with the aid of a fan. The microstructures of the pre-deformation samples were then compared to the as-extruded microstructure.

5.2.1 Experimental Results

Figure 5.2 displays the EBSD inverse pole figure (IPF) map of the as-extruded material before heating and compression. The IPF map contains 941 grains in a 40x40μm scan area. The as-extruded material has an average measured mean linear intercept grain diameter of 1.07μm and the number fraction of grains containing twins is 0.35. Figure 5.3 shows the IPF maps of the pre-deformation samples heated to the 4 different test temperatures. Figure 5.4 plots the average grain size of the 4 pre-deformation samples compared to the as-extruded. The grain size distribution of the

as-extruded material along with pre-deformation samples at 1323K (1050˚C), 1298K (1025˚C), 1269K (996˚C), 1241K (968˚C) are shown in Figure 5.5. Despite a small change in the average grain size during ramp-up to different temperatures, the grain size distributions do not qualitatively change.

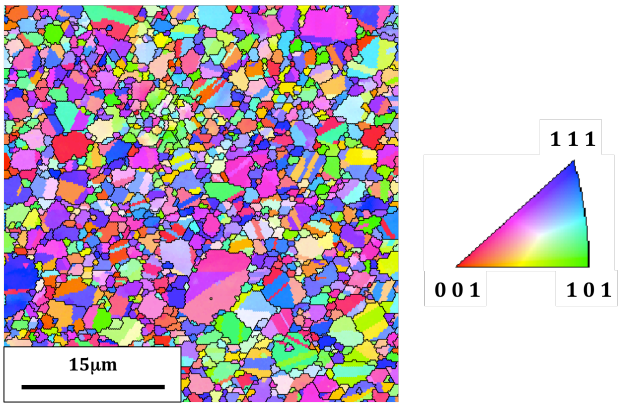

Figure 5.2: Inverse pole figure (IPF) plot of as-extruded René 88DT.

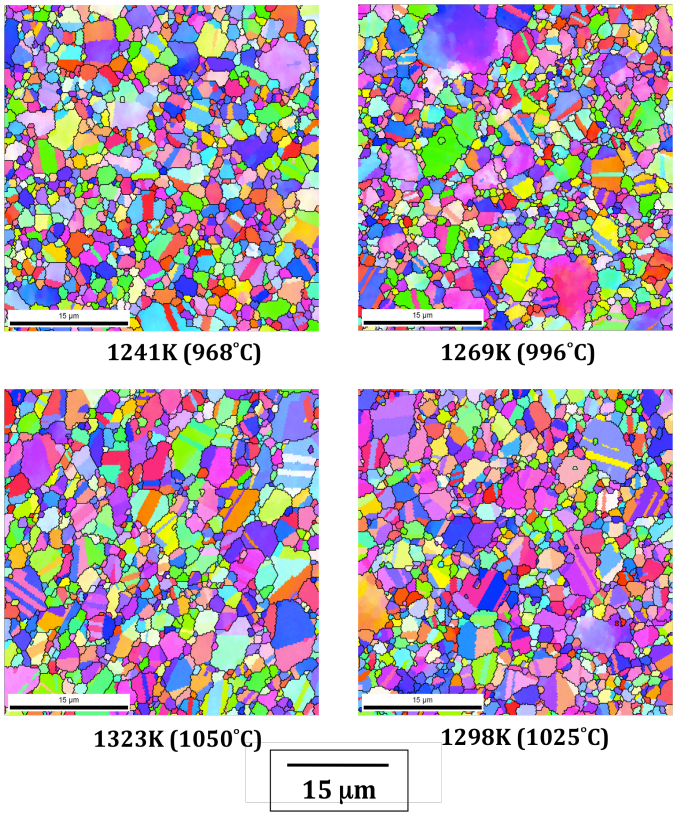

Figure 5.3: IPF maps showing René 88DT microstructure after ramp-up to target temperature before deformation.

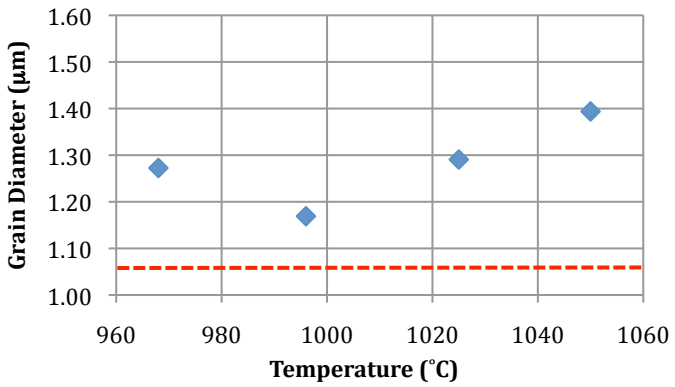

Figure 5.4: Average grain diameter of pre-deformation samples. As-extruded grain size is indicated by red line.

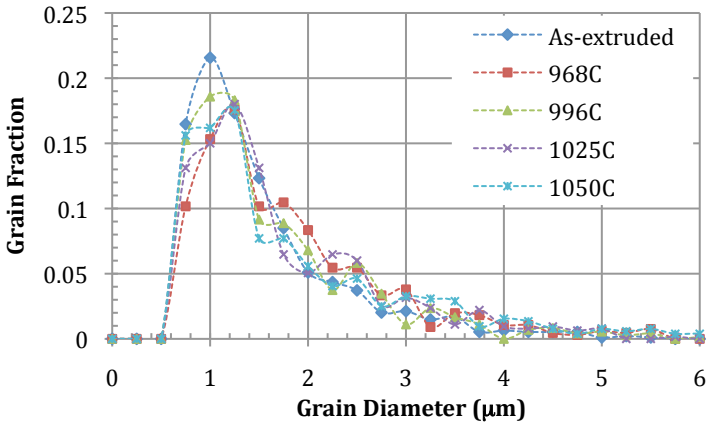

Figure 5.5: Grain diameter distribution of as-extruded René 88DT compared to pre-deformation samples of different temperatures.

The number fraction of grains containing twins and the area fraction of grains without twins are shown in Figures 5.6 and 5.7, respectively. The plots show that as fraction of grains containing twins increases, the area fraction of grains containing twins also increases suggesting that the grains which twin are the larger grains.

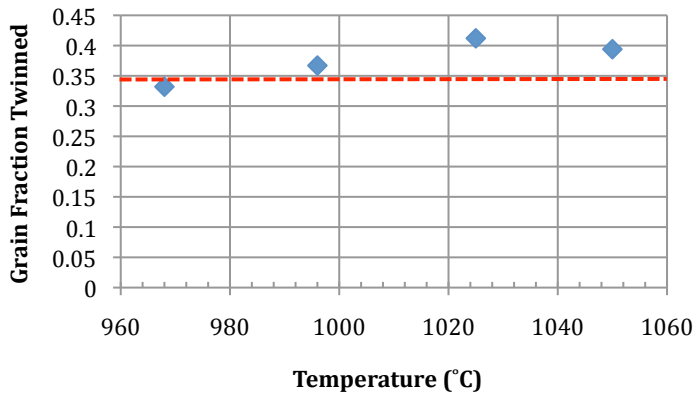

Figure 5.6: Fraction of grains containing twins as a function of pre-deformation temperature. As-extruded level shown by red line.

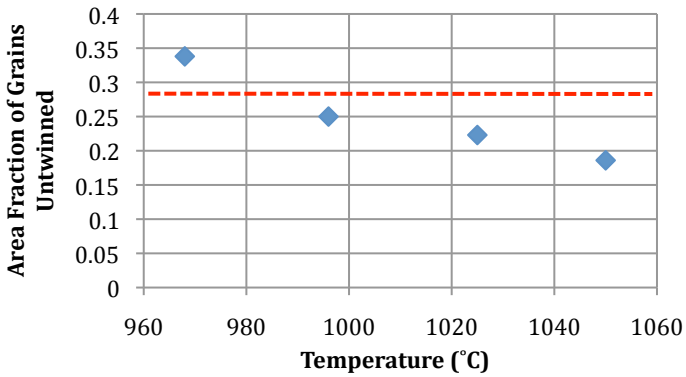

Figure 5.7: Area fraction of grains untwinned as a function of pre-deformation temperature. As-extruded level shown by red line.

5.2.2 Discussion

Experiments show that grain coarsening occurs during pre-deformation heat-up of René 88DT samples. The amount of grain coarsening varies depending on hold temperature. The coarsening of the microstructure is attributed to the dissolution of γ' since γ' particles create a significant amount of pinning force against grain growth. But as the volume fraction of γ' decreases during initial heating of samples, the pinning force against grain growth decreases, and therefore grain growth is allowed to occur. To clearly understand grain coarsening, a detailed understanding of the equilibrium γ' volume fraction is needed.

5.2.2.1 Equilibrium γ' Volume Fraction

The equilibrium volume fraction of γ' particles (f_{eq}) corresponds to a temperature (T) for René 88DT was empirically measured and is given by [61]:

$$f_{eq} = f_{\max}\left(\frac{1-e^{-7250\left[\frac{T_s-T}{T_sT}\right]}}{1-68e^{-\frac{7250}{T}}}\right) \qquad [5\text{-}1]$$

where f_{max} is the maximum volume fraction of γ' and T_s is the γ' solvus temperature. The equilibrium volume fraction of γ' as a function of temperature is shown in Figure 5.8. The volume fraction of γ' decreases significantly from 1241K (968˚C) to 1323K (1050˚C), going from 0.25 to 0.14, respectively. Therefore, less γ grain coarsening and a smaller average grain size is expected at lower test temperatures due to the increased pinning force from γ' particles. However, experimental results show that the average grain size at 1241K (968˚C) does not follow this trend and is larger than expected. This discrepancy could be due to the larger particle size of primary γ' at 1241K (968˚C) due to the slower dissolution rate and higher f_{eq}.

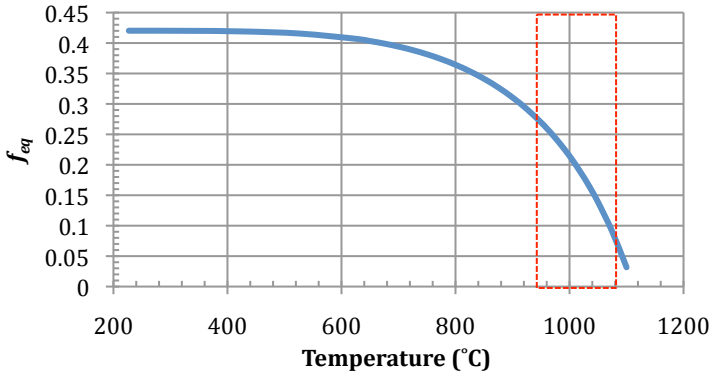

Figure 5.8: René 88DT equilibrium γ' volume fraction as a function of temperature. Red box outlines testing temperatures.

5.2.2.2 γ' Dissolution Rate

The dissolution kinetics of γ' below the solvus follow the general form given by Humphreys [62] such that the time dependent volume fraction of γ' (*f*) can be described as:

$$f = f_{eq} + \left(f_0 - f_{eq}\right)\exp\left(-Kt^n\right) \qquad [5\text{-}2]$$

where f_{eq} is the temperature dependent equilibrium volume fraction, and *K* and *n* are temperature dependent material constants. Wang *et al.* calculated *K* and *n* for binary Ni-Al alloys and reported values of 0.6132/s and 0.5171 respectively [63]. Using those values, it has been determined that dissolution of γ' to the equilibrium volume fraction below solvus takes less than 40s, assuming a log-normal distribution of γ' particles. The dissolution kinetics would be even faster if γ' particle sizes fit a normal distribution. Therefore, during the ramp-up to test temperature and the subsequent hold at test temperature for 2 minutes, significant γ' dissolution occurs, with γ' volume fraction approaching the equilibrium volume fraction in less than 40s at temperatures near the solvus temperature. Due to the fast dissolution rate of γ', it is assumed that the γ' volume fraction has already reached f_{eq} during the hold at test temperature before deformation and that the γ' volume fraction remains unchanged during deformation.

5.3 Temperature and Strain Rate Dependent Microstructural Evolution

Three separate sets of experiments were conducted on René 88DT to determine the microstructural evolution during high temperature compression. The first set of experiments was conducted to determine the effects of temperature and

strain rate on microstructure during compression. The second set of experiments was conducted to determine the evolution of microstructure as a function of strain for various strain rates. The final set of experiments was conducted to determine the presence and magnitude of superplasticity-enhanced grain growth during high temperature deformation of René 88DT.

5.3.1 Experimental Results

The first set of experiments was conducted at 4 different test temperatures, 1323K (1050˚C), 1298K (1025˚C), 1269K (996˚C), 1241K (968˚C) and with 4 different strain rates, 0.00032/s, 0.0032/s, 0.032/s, 0.1/s. All samples compressed to 110% true strain. The flow curves were shown in Figures 4.1 – 4.4. Figure 5.9 displays the EBSD IPF maps of René 88DT compressed in this set of experiments. The as-extruded IPF map is shown on the right for comparison. The IPF maps illustrate that significant grain refinement occurs during deformation at higher strain rates when compared to the as-extruded microstructure. On the contrary, the IPF maps illustrate that grain growth occurs during deformation at slower strain rates for all temperatures. Furthermore, the microstructure consistently becomes finer when test temperature decreases for all imposed strain rates. Figure 5.10 shows these trends by displaying the average grain size after compression as a function of strain rate and temperature.

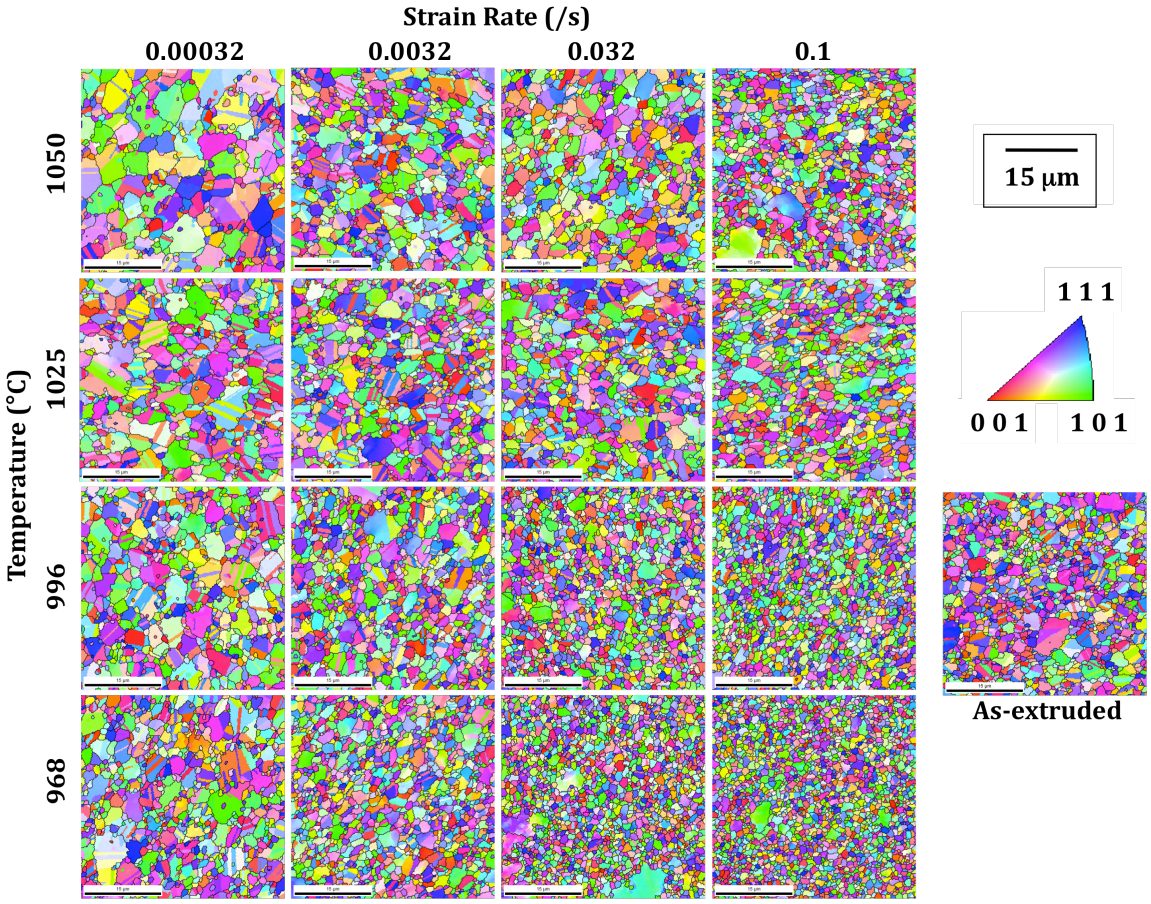

Figure 5.9: IPF plot of René 88DT compressed at 4 different temperatures with 4 different strain rates, as labeled by the vertical and horizontal axis respectively. The as-extruded IPF plot of shown on the right side.

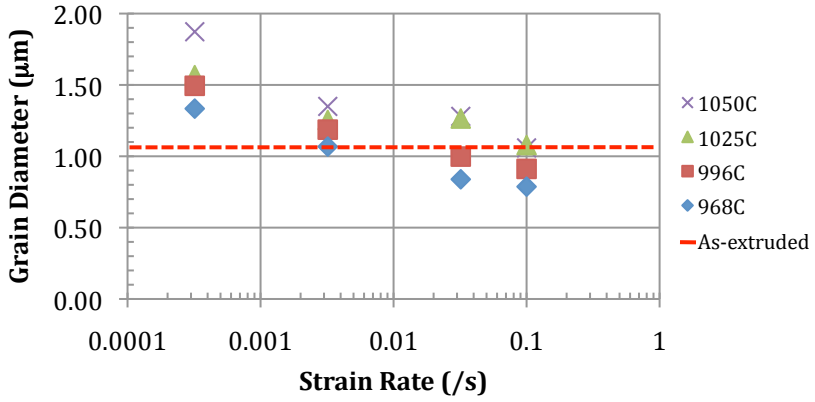

Figure 5.10: Average grain diameter of René 88DT plotted as a function of compression strain rate for varying test temperatures. As-extruded average grain diameter is indicated by dashed red line.

The grain diameter distributions of René 88DT compressed at various strain rates are shown in Figures 5.11 – 5.14. When compared to the as-extruded grain

diameter distribution, the grain diameter distributions evolve as a function of strain rate and temperature as follows:

1. Grain diameter distributions narrow as strain rate increases for all test temperatures.
2. Grain diameter distributions for samples compressed at slow strain rates are broader than the as-extruded grain diameter distribution.
3. Grain diameter distributions for samples compressed at faster strain rates are narrower than the as-extruded grain diameter distribution.
4. The grain diameter distributions broaden as temperature increase for samples compressed at the same strain rate.

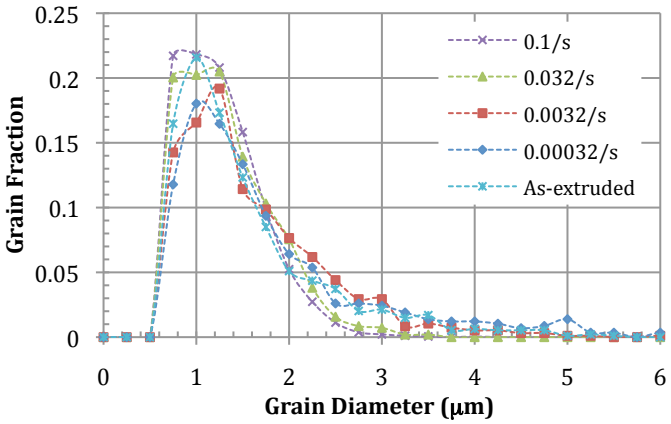

Figure 5.11: Grain diameter distribution for René 88DT compressed at 1241K (968˚C).

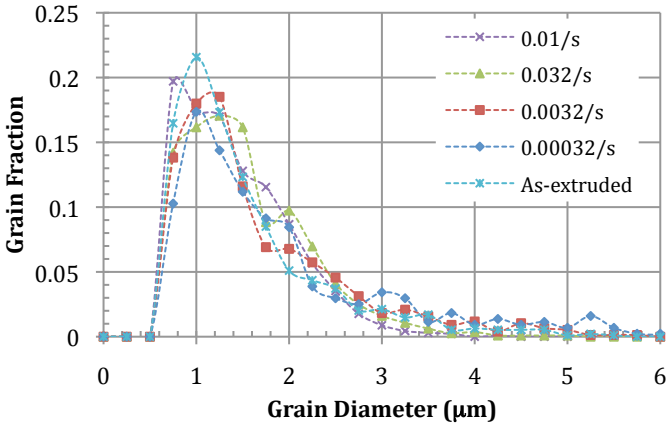

Figure 5.12: Grain diameter distribution for René 88DT compressed at 1269K (996˚C).

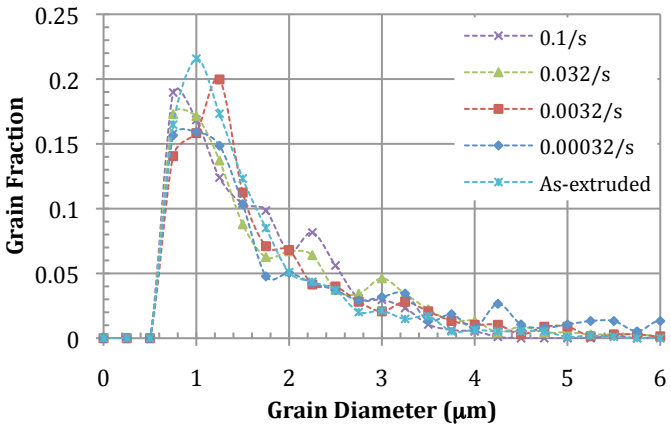

Figure 5.13: Grain diameter distribution for René 88DT compressed at 1298K (1025˚C).

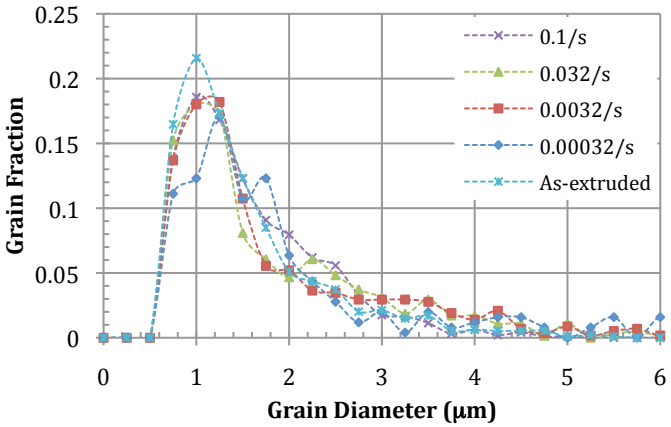

Figure 5.14: Grain diameter distribution for René 88DT compressed at 1323K (1050˚C).

Figure 5.15 shows the fraction of grains containing twins after compression of René 88DT. It shows that the fraction of grains containing twins reduces as compared to the as-extruded fraction when compressed at high strain rates. Furthermore, the magnitude of the reduction in fraction containing twins is higher at the lowest test temperatures. Deformation at the slowest strain rate (0.00032/s) yields a microstructure with a higher fraction of grains containing twins. The area fraction of grains containing twins as a function of strain rate as shown in Figure 5.16 shows similar trend as the fraction of grains containing twins graph. By using the area fraction of grains containing twins, the number fraction of grains containing twins, the scan area, and the total number of grains scanned, the average grain size of the

twinned and untwinned grains can be calculated. Figures 5.17 – 5.20 show the average twinned and untwined grain sizes as a function of strain rate for different test temperatures. As it can be seen, the average grain size of the twinned grains is always larger than the average grain size of the untwinned grains. Furthermore, the average twinned grain size increases with decreasing strain rate and increasing temperature while the average untwinned grain size remains relatively constant around 1.5μm, which is slightly larger than the as-extruded untwinned grain size of 1.36μm, at all test temperatures and strain rates. When compared to the as-extruded twinned grains, which have an average grain diameter of 3.05μm, the average twinned grains are larger during deformation at the lower strain rates. But during deformation at higher strain rates, the grains are refined as compared to the as-extruded grain size.

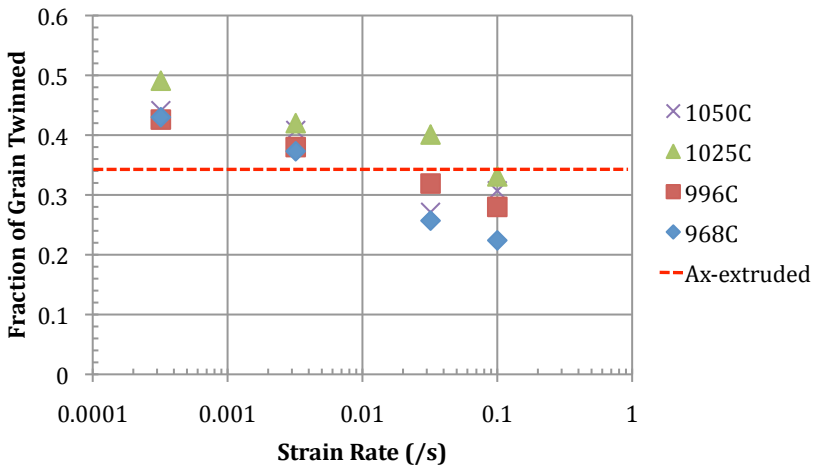

Figure 5.15: Fraction of grains twinned of René 88DT after deformation at various temperatures and strain rate. Imposed strain is 110% true strain. As-extruded level is shown by red line.

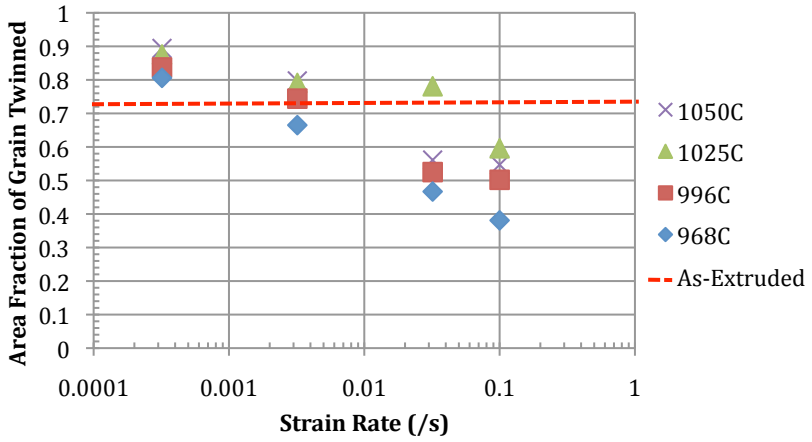

Figure 5.16: Area fraction of René 88DT twinned after deformation at various temperatures and strain rates. Imposed strain is 110% true strain. As-extruded level is indicated by red line.

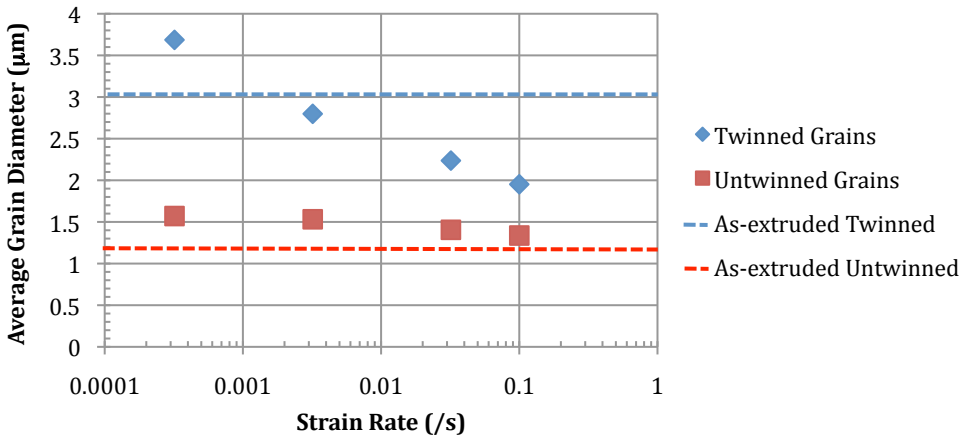

Figure 5.17: Average grain diameter of twinned and untwinned grains compressed at 1241K (968˚C).

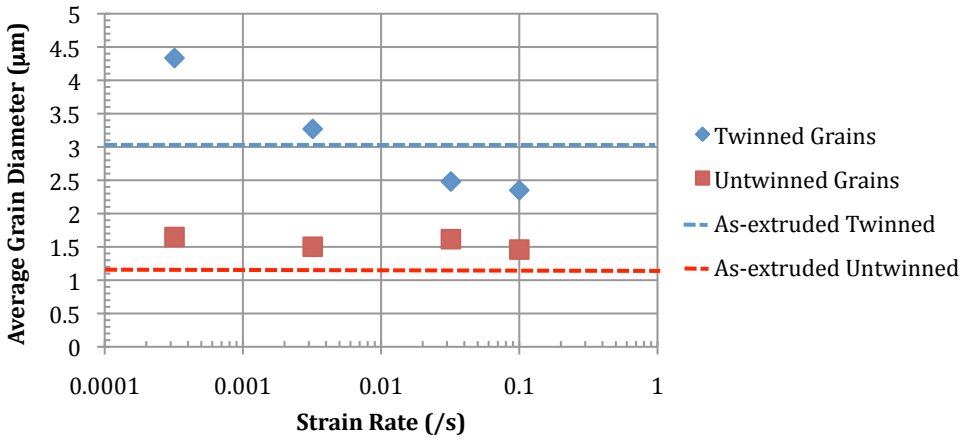

Figure 5.18: Average grain diameter of twinned and untwinned grains compressed at 1269K (996˚C).

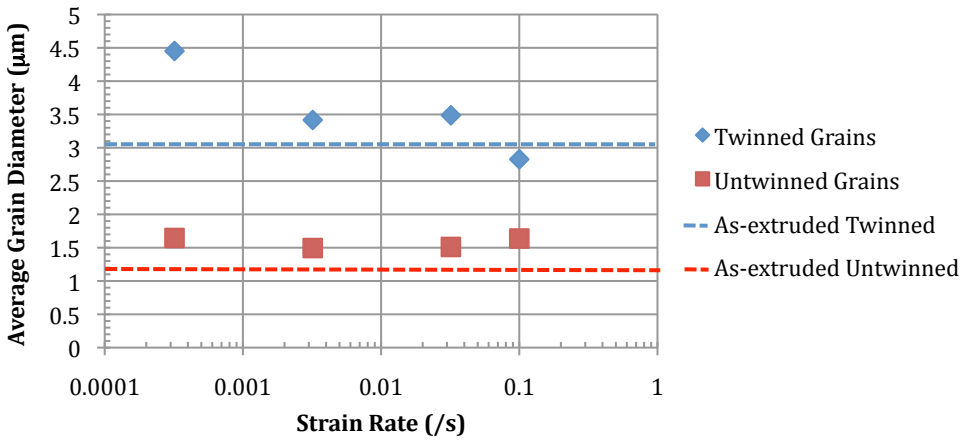

Figure 5.19: Average grain diameter of twinned and untwinned grains compressed at 1298K (1025˚C).

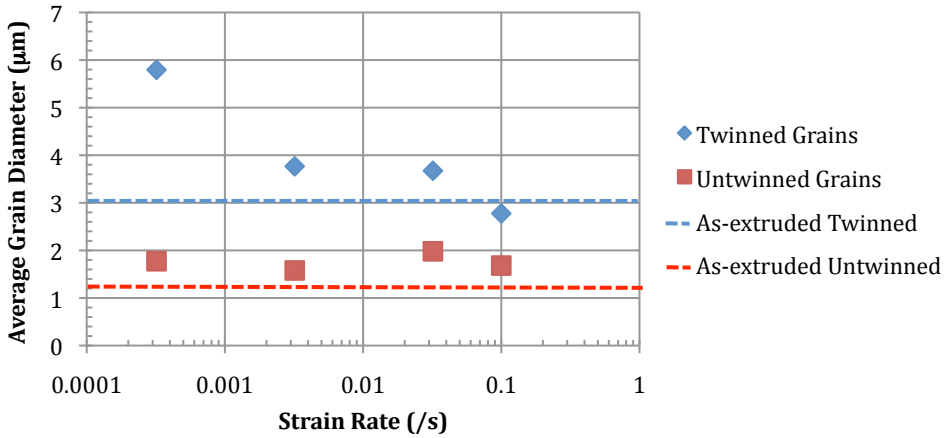

Figure 5.20: Average grain diameter of twinned and untwinned grains compressed at 1323K (1050˚C).

5.3.2 Discussion

During high temperature deformation of René 88DT at 4 different strain rates and 4 different temperatures, René 88DT microstructure evolves as a function of both strain rate and temperature. During deformation at low strain rates where superplastic deformation occurs (0.00032 and 0.0032/s), grain coarsening corresponds with broadening of the grain size distribution and increasing twinned grain fraction. During deformation at high strain rates where power creep deformation and dynamic recrystallization is expected to dominate (0.032/s and 0.1/s), grain refinement

corresponds to a narrowing of the grain size distribution and a decrease in the fraction of grains twinned.

5.3.2.1 Slow Strain Rate Grain Size Distribution

As mentioned above, slow strain rate deformation of René 88DT at elevated temperature results in a broadening of the grain size distribution as compared to the as-extruded microstructure. All of the measured grain size distributions show a high fraction of grains with diameter between 0.5 and 1.5μm, with a peak fraction near 1μm. As the grain size distribution broadens, the peak does not shift, but a secondary peak of larger diameter becomes evident indicating that there are two populations of grains with different time evolution (Figure 5.14). The larger and smaller diameter population are of course the γ and primary γ' grains, respectively. Though the two populations of grains are visually evident in the grain size distributions, the mean diameter and volume fraction of each population cannot be calculated due to the overlap of the two distributions and the evolution of both distributions during deformation. Furthermore, ordered phases such as γ' cannot be distinguished from the matrix phase using Kikuchi patterns of the EBSD technique. Therefore, due to the bi-modal evolution of the overall grain structure, the grain size distributions do not accurately fit any standard distribution curves.

5.3.2.2 γ' Coarsening Rate

During high temperature deformation of René 88DT, the high volume fraction of γ' (between 0.14 – 0.25) stabilizes the microstructure, pins grain boundaries, and slows the coarsening of the γ grains. The coarsening of the microstructure observed during slow strain rate compression in the experiment can occur due to the coarsening

of the primary γ' and the dissolution of γ' to the equilibrium volume fraction, resulting in reduction in number of pinning particles, therefore reducing the pinning force of the primary γ' population. The coarsening rate of primary γ' has been measured on the same material by E Payton et. Al [2]. The coarsening rate is reported to follow LSW-type cubic coarsening in the form of [2]:

$$d = \sqrt[3]{k_0 t \exp\left(\frac{Q_c}{RT}\right) + d_0^3} \qquad [5\text{-}3]$$

where Q_c = 49.56kJ/mol is the activation energy, k_0 = 4.5 x 10^{-5}μm^{3}K/s is a material constant, and d_0 = 1μm is the estimated initial average primary γ' diameter. This solution fit to experimental results for γ' particle sizes measured by E. Payton show a very slow coarsening rate as shown by Figure 5.21, which indicates that average grain size coarsening occurs primarily by reduction of Zener pinning forces as a result of γ' dissolution to equilibrium volume fraction before deformation starts.

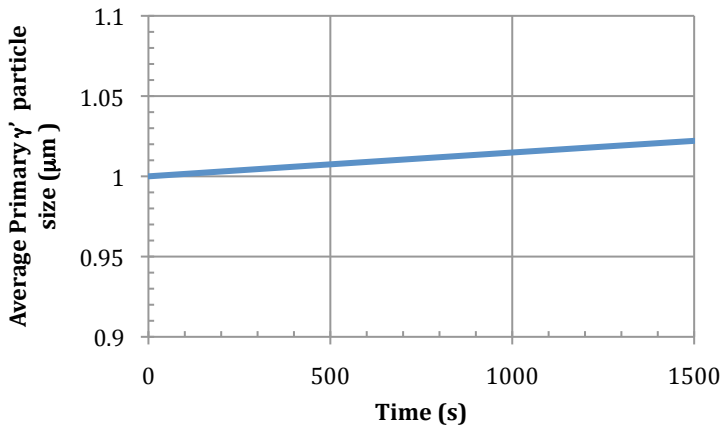

Figure 5.21: Primary γ' coarsening rate of René 88DT according to LSW-type coarsening equation presented by E. Payton [2].

5.3.2.3 The γ Grain Size: the Zener Limit

The reduction in volume fraction of γ' reduces the number and volume fraction of Zener pinning particles, therefore increasing the Zener pinned limit grain

size of γ. The γ grain size limit (D_{lim}) has been modeled by Song *et al.* for Ni-base superalloys [64]. They found that the Zener pinned limit γ grain size could be expressed as:

$$\frac{1}{D_{\lim}} = \frac{0.45 f_{eq}^{0.56}}{r} + \frac{1}{51} \qquad [5\text{-}4]$$

by fitting experimental data of γ grain size after heat treatment for 300min at temperatures below the γ' solvus, assuming that the γ grain size has reached the Zener pinned limit after 300min at temperature. In the solution, r and f_{eq} are the size and equilibrium volume fraction of γ'particles, respectively. This solution accounts for Zener drag of γ' particles as well as that of inert precipitates such as carbides and borides. Combining equations 5-2 and 5-4, a temperature dependent Zener limit γ grain size can be calculated assuming that the γ' has equilibrated at the equilibrium volume fraction, as shown in Figure 5.22.

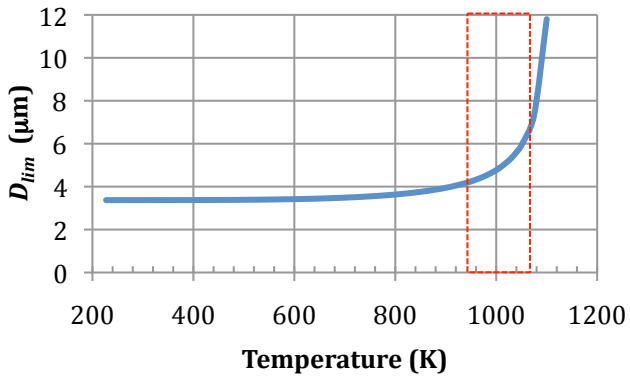

Figure 5.22: René 88DT Zener limit γ grain size as a function of temperature dependent equilibrium γ' volume fraction. Red box outlines test temperature range.

5.3.2.4 Evolution of Grain Twinning

EBSD analysis shows that the fraction of grains containing twins evolves as a function of both temperature and strain rate and follows a power-law equation as

shown in Figure 5.13. The figure displays fraction of grains twinned for samples compressed at different strain rates, all at 1298K (1025˚C).

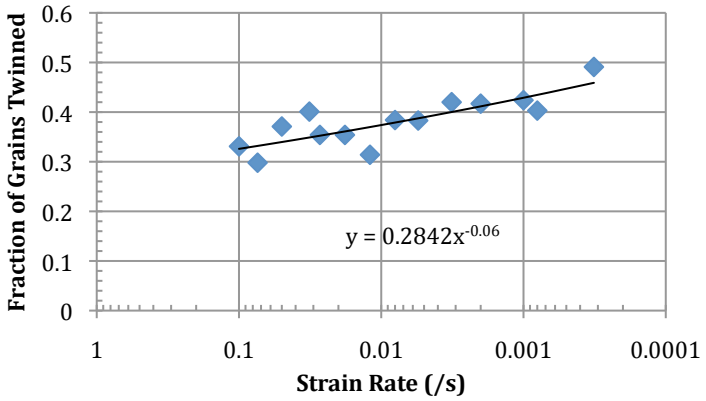

Figure 5.23: Fraction of grains twinned as a function of strain rate for René 88DT compressed at 1298˚K (1025˚C).

The fraction of grains twinned follows a power-law in the form:

$$f_{twin} = k(T)\dot{\varepsilon}^{n} \qquad [5\text{-}5]$$

where *k(T)* is the temperature dependent twin fraction constant, and *n* is the power-law exponent, which equals -0.06.

During high temperature compression at slower strain rates where grain growth occurs, grain growth is limited to those grains that contain twins while the average size of grains without twins stay constant at 1.5μm. Since γ grains coarsen during high temperature deformation and γ' coarsening is negligible, this suggests that the majority of the γ grains contain twins. Therefore, average untwinned grain size during deformation at the slowest strain rate (0.00032/s) should be comparable to the Zener limit γ grain size since compression at this strain rate to a true strain of 110% takes 2031s. Figure 5.24 compares the temperature dependent Zener limit γ grain size to the average twinned grain size after deformation at 0.00032/s strain rate to 110% true strain (compression time = 2031s). The twinned grain size follows the

trend of calculated Zener limit γ grain size. The minor deviation of measured average twinned grain size as compared to the Zener limit γ grain size is most likely due to the difference in time-at-temperature; the Zener limit grain size was calculated for samples held at temperature for 300min while twinned grain size was measured for samples held at temperature for 22min, which may not be enough time for the limit grain size to be reached at lower temperatures where atomic diffusivity is lower. Nevertheless, the data suggest that during deformation at slow strain rates when recrystallization does not occur, the majority of the grains that twinned are γ grains and the majority of grains untwinned are γ'. Furthermore, since the as-extruded material contains a large fraction of twinned grains (0.43) and the increase in average twinned grain size during compression corresponds to a decrease in fraction of grains untwinned, it is obvious that the twinning of grains was a result of processing preceding the high temperature deformation and that no significant fraction of grains twin during deformation at strain rates of 0.00032/s and 0.0032/s.

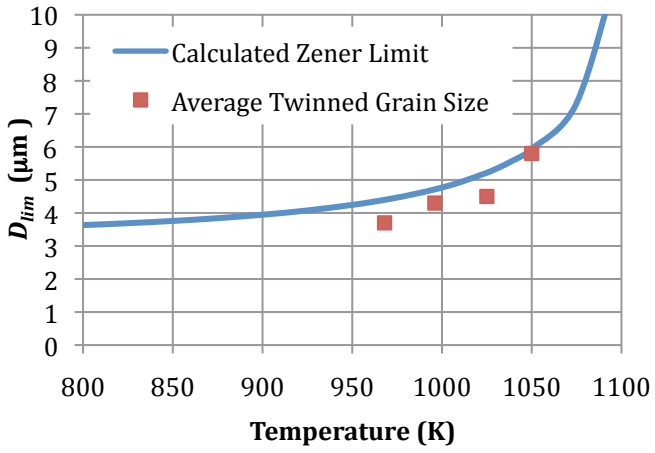

Figure 5.24: Zener limit of γ grain size as a function of temperature assuming that equilibrium γ' volume fraction has been reached compared to the average grain size of twinned grains after deformation at 0.00032/s strain rate at various temperatures.

5.3.2.5 Dynamic Recrystallization During High Strain Rates

During high temperature compression at higher strain rates (0.032 and 0.1/s) where power-law creep deformation is expected to be dominant, the microstructure of René 88DT becomes finer; the average grain diameter decreases as compared to the as-extruded grain size. Grain size refinement during deformation of metallics usually indicates dynamic recrystallization as a recovery mechanism. Evidence of dynamic recrystallization has already been seen in the flow stress behavior during compression where strain softening is observed at high strain rates. Strain softening corresponds to a decrease in grain size as a result of dynamic recrystallization. The size of the recrystallized grains depends both on strain rate and temperature; the recrystallized grain size increases with increasing temperature and decreasing strain rate. Therefore, the smallest grain sizes are expected at the highest strain rate (0.1/s) and the lowest temperature, 1241K (968˚C). At those testing conditions, the final measured average grain diameter indeed finer, and the finest being 1.24μm, which is 40% smaller than the as-extruded grain size. The grain size distribution of René 88DT also narrows compared to the as-extruded during compression at the higher strain rates (0.032 and 0.1/s). This phenomenon is again attributed to the dynamic recrystallization that is evident during deformation at these strain rates.

The low fraction of grains containing twins during deformation at high strain rates also suggests that dynamically recrystallized grains form without twins as during deformation at high strain rates, the area fraction of grains untwinned far exceeds the volume fraction of γ'.

5.4 Strain Dependent Microstructural Evolution

To examine the strain dependence of the microstructural evolution, the second set of compression tests on René 88DT was conducted at 1298K (1025˚C) using different strain rates (0.001, 0.0055, 0.018, 0.05/s) and strain increments of 0.1 engineering strain from 0 – 0.5 strain.

5.4.1 Experimental Results

The IPF plots of this set of experiments are shown in Figure 5.25, where each column represents samples compressed at a different strain rate and each row represents samples compressed to a different strain. The scale bar and the as-extruded microstructure are shown on the right side of the figure. It can be seen that as both strain and strain rate increases, the grain size after compression decreases. The finest microstructure after compression is observed in the sample compressed at 0.05/s strain rate to an imposed engineering strain of 0.5. The samples compressed at a strain rate of 0.001/s showed the most coarse microstructure. The average grain size as a function of strain is shown in Figure 5.26; the graph shows an evolution of grain refinement as a function of strain for samples compressed at 0.05 and 0.018/s strain rates. The samples compressed at 0.0055 and 0.001/s shows a fluctuating grain size with some grain coarsening as a function of strain.

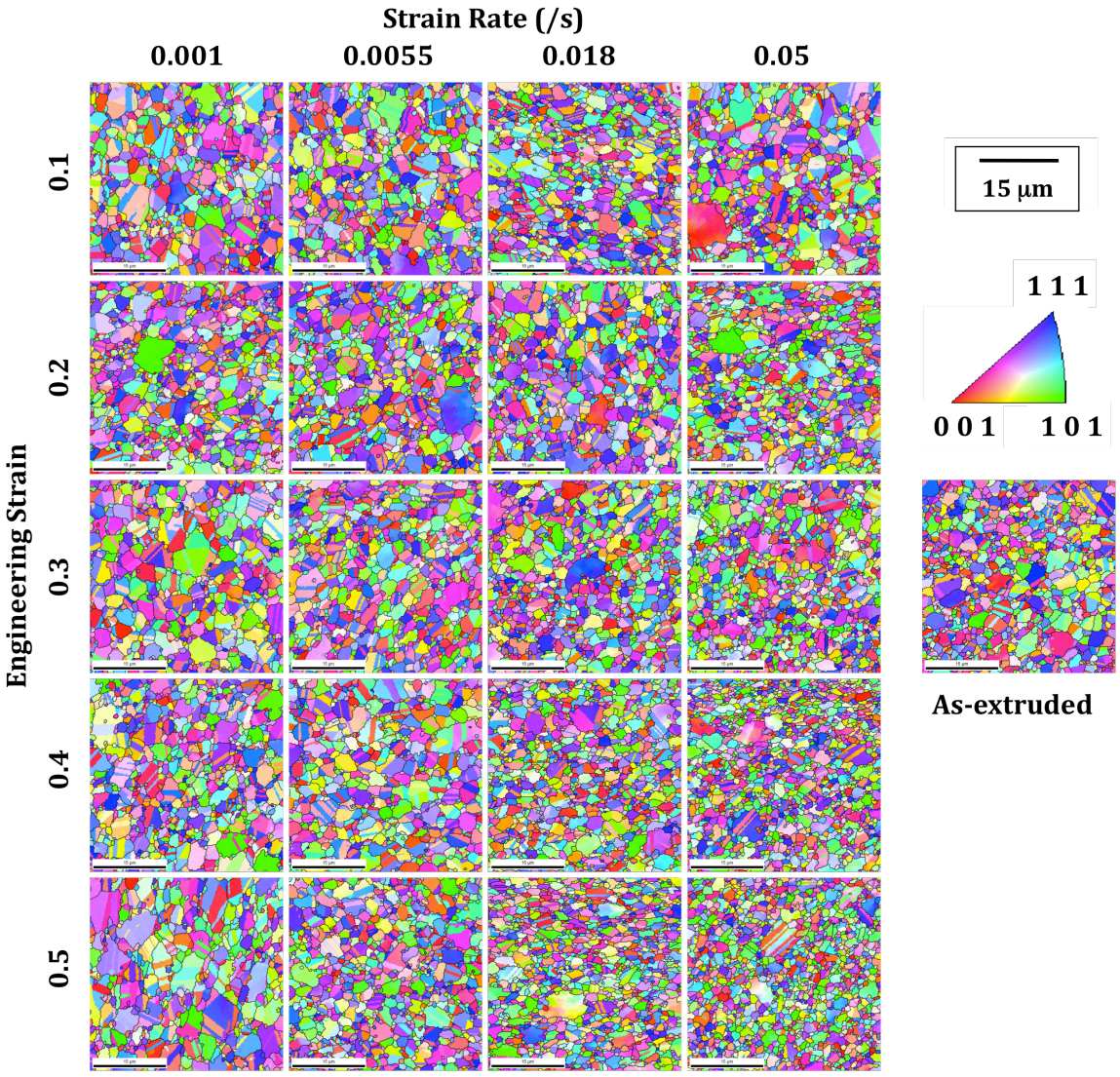

Figure 5.25: IPF plot of René 88DT compressed at different strain rates to different engineering strain. All samples test temperature is 1298K (1025˚C). The as-extruded microstructure is shown on the right.

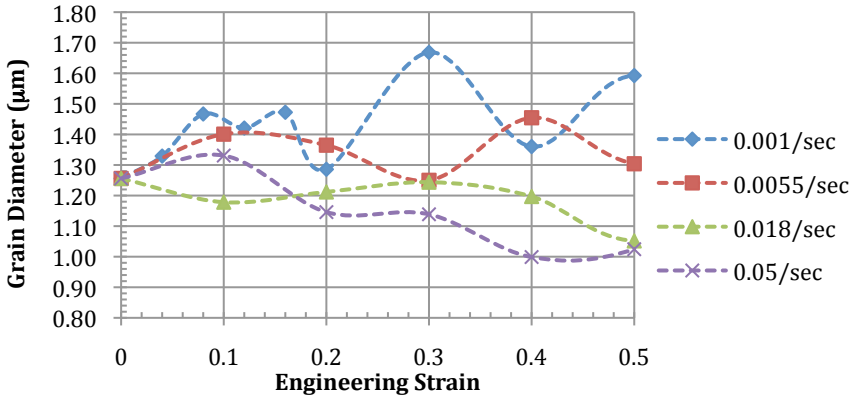

Figure 5.26: Average grain diameter as a function of engineering strain for René 88DT compressed at varying strain rates at 1298K (1025˚C).

Figure 5.27 plots the fraction of grains containing twins as a function of strain for the 4 strain rates in this experimental set. The figure shows that the fraction of grains containing twins fluctuates around the as-extruded fraction for all test conditions. The fluctuations become larger and favor fractions greater than the as-extruded level at lower strain rates. Figure 5.24 – 5.31 plot the average twinned and untwinned grain sizes as a function of engineering strain for the 4 strain rates. The untwinned grain size again stays relatively constant for all test parameters. The average untwinned grain size fluctuates around the as-extruded grain size (1.54μm) during compression at 0.0055, 0.018, and 0.05/s strain rates. The twinned grain size coarsening as strain increases during compression at 0.001/s and 0.0055/s strain rates. At 0.018/s and 0.05/s strain rates, the twinned grain size refines as strain increases. Grain refinement seems to initiate at a lower strain during deformation at 0.001/s as compared to initiation of grain refinement at 0.018/s strain rate. This indicates that the critical strain to initiate dynamic recrystallization is strain rate dependent.

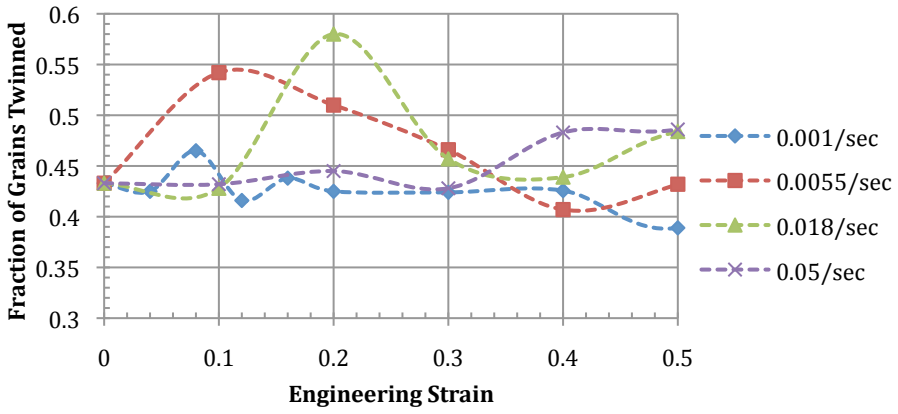

Figure 5.27: Fraction of grains twinned as a function of engineering strain for René 88DT compressed at varying strain rates at 1298K (1025°C).

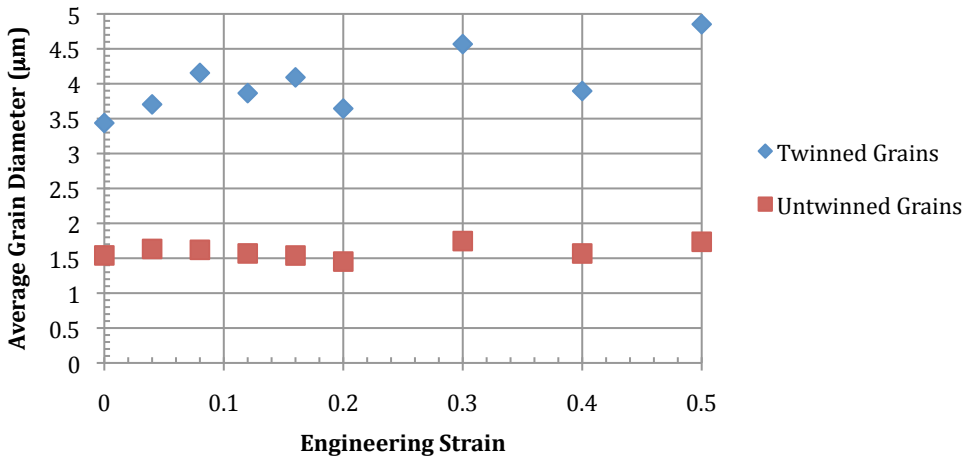

Figure 5.28: Average grain diameter twinned and untwinned grains as a function of strain for René 88DT compressed at 0.001/s at 1298K (1025˚C).

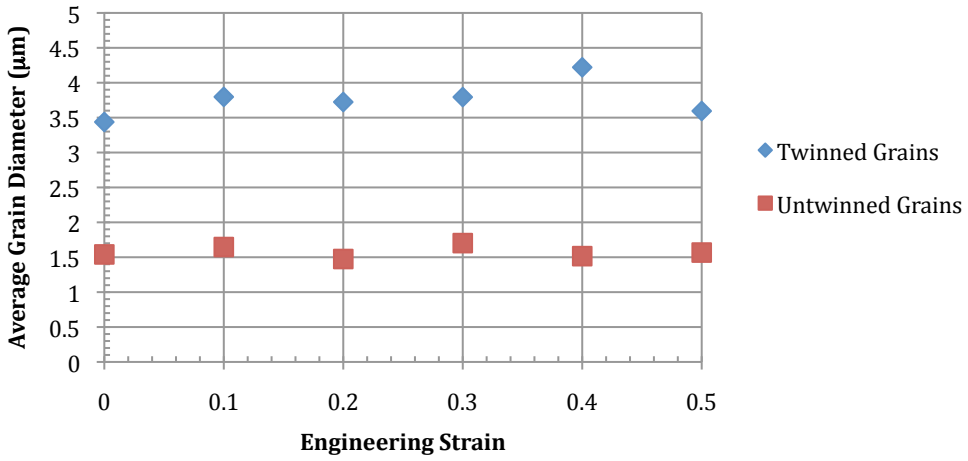

Figure 5.29: Average grain diameter twinned and untwinned grains as a function of strain for René 88DT compressed at 0.0055/s at 1298K (1025˚C).

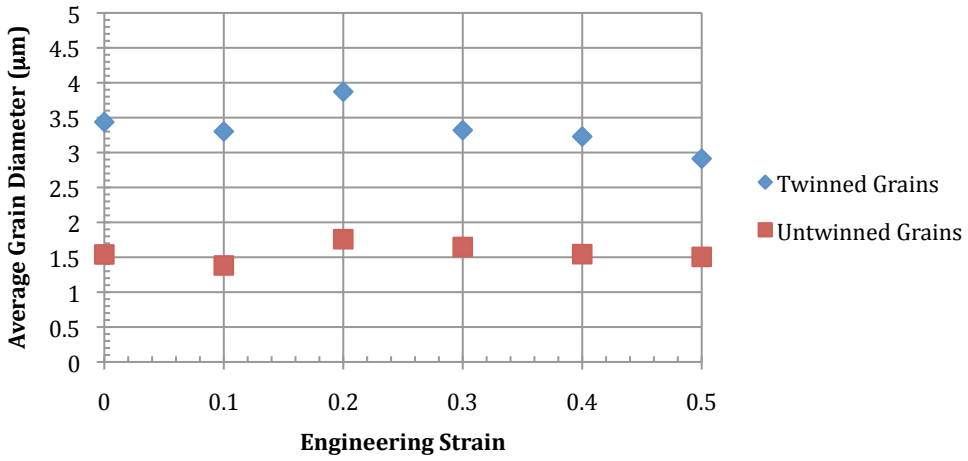

Figure 5.30: Average grain diameter twinned and untwinned grains as a function of strain for René 88DT compressed at 0.018/s at 1298K (1025˚C).

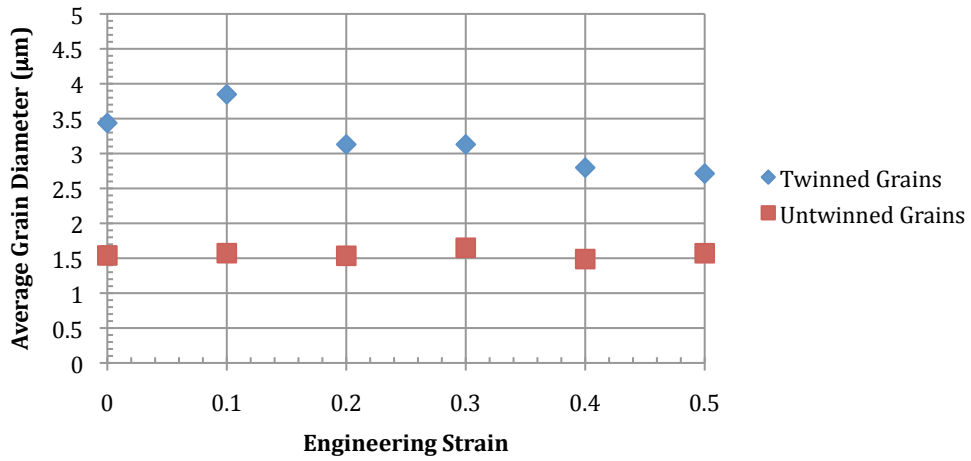

Figure 5.31: Average grain diameter twinned and untwinned grains as a function of strain for René 88DT compressed at 0.05/s at 1298K (1025˚C).

5.4.2 Discussion

René 88DT samples compressed to 0.1 strain increments at 1298K (1025˚C) show that both grain refinement at high strain rates and grain coarsening at low strain rates occur gradually during straining. The gradual decrease in grain size during deformation at higher strain rates indicates that dynamic recrystallization occurs not in a single wave but rather either by multiple waves or in steady state. The coarsening and refinement of the grain structure again corresponds to increases and decreases in the fraction of grains containing twins, respectively. The average size of grains that are untwinned stays almost constant at ~1.5μm while the average size of the grains that are twinned increase during deformation at slower strain rates, and decrease during deformation at high strain rates. The average twinned grain size fluctuates around the ax-extruded size (3.35μm) during compression at intermediate strain rates (0.0055/s, 0.018/s) indicating that dynamic recrystallization is occuring. The fraction of grains containing twins shows no obvious trend as a function of strain at any strain rate; the fraction of grains containing twins fluctuates around the as-extruded fraction as strain progresses.

5.5 Superplasticity Enhanced Grain Growth

The René 88DT microstructure coarsens during deformation at slow strain rates (<0.0032/s). At these strain rates, deformation occurs by superplasticity, as evidenced by a measured strain rate sensitivity coefficient larger than 0.4. Studies have shown that enhanced grain growth can result from superplastic deformation. To look for evidence of superplasticity-enhanced grain growth in René 88DT, samples were compressed at different superplastic strain rates (0.001, 0.002, 0.0032) at 1298K (1025˚C), to discrete time intervals to measure grain growth rates as compared to grain growth rate during static annealing.

5.5.1 Experimental Results

Figure 5.32 shows the average grain size progression as a function of time of René 88DT compressed at 1298K (1025˚C) using 0.002/s, 0.001/s, and no imposed strain. The grain coarsening rates for up to 100s compression for samples compressed at 0.002/s and 0.001/s are similar when compared to the static grain growth rate.

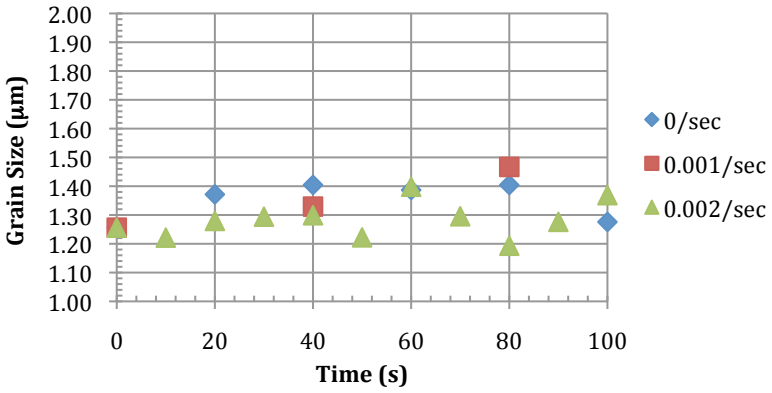

Figure 5.32: Time interval grain size evolution during compression at different superplastic strain rates.

5.5.2 Discussion

René 88DT shows comparable grain coarsening rates for samples compressed at 0.001/s, 0.002/s and no imposed strain at 1298K (1025˚C). Payton has shown that the grain coarsening rate during deformation is sensitively dependent on the volume fraction of γ' [2]. Dissolution of γ' occurs quickly, reaching the temperature dependent equilibrium volume fraction in less than 40s as the samples are held at test temperature before deformation starts. Therefore, grain growth occurs quickly initially as γ' dissolves. As the γ grain size approach the Zener pinned limit, the grain growth rate slows substantially. Therefore, a model of superplasticity enhanced grain growth would need to account for the pinning force of γ' particles as well as the evolving volume fraction of γ'. The proposed model for superplasticity enhanced grain growth will be presented in Chapter 8.

5.6 Chapter Summary

In this chapter, the microstructural evolution of René 88DT before and during high temperature compression was studied using the EBSD technique in the SEM. Testing conditions ranged from temperature (T) = 1241K (968˚C) to 1323K (1050˚C), strain rate ($\dot{\varepsilon}$) = 0.00032/s to 0.1/s, and true strain up to 1.1. It was shown before deformation during thermal transients:

1. The rate of γ' dissolution at test temperatures is rapid enough that the equilibrium γ' volume fraction is reached in less than 1min.
2. The equilibrium volume fraction of γ' at test temperatures decreases from 0.25 to 0.14 as temperature increases from 1241K (968˚C) to 1323K (1050˚C).

3. γ’ dissolution and the subsequent decrease in γ’ volume fraction causes grain coarsening before and during deformation.
4. Area fraction of grains containing twins decreases as temperature increases.

Analysis of microstructure evolution during high temperature deformation indicated that:

1. Average grain size increases as deformation temperature increases and strain rate decreases.
2. Fraction of grains containing twins and area fraction of twinned grains both decrease as strain rate increases.
3. The average grain size of grains containing twins decrease as strain rate increases, but the average grain size of untwinned grains remain steady throughout the entire range of test conditions.
4. The average twinned grain size is much larger than the average untwinned grain size.
5. Minimal γ’ coarsening occur at test temperatures.
6. The experimentally measured average grain size of twinned grains follow the same trend as the calculated Zener limit grain size indicating that majority of twinned grains are γ grains and that the majority of the untwinned grains are γ’.
7. Grain refinement is observed during deformation at higher strain rates while grain coarsening is observed during deformation at lower strain rates.

8. Grain refinement at higher strain rates indicates the occurrence of dynamic recrystallization.

Using EBSD to analyze grain structure evolution has yielded clearer understanding of the microstructural response to high temperature deformation for René 88DT. The grain size and twin data presented throughout this chapter will be used to derive deformation models in chapter 7 of this study. The deformation and microstructural evolution models derived from this data will yield a clearer understanding of the boundaries of different deformation mechanisms and the effects of associated microstructure responses during high temperature superplastic forging of Ni-base superalloy disks.